Strain Tunability of the
Excitonic Spectrum in Phosphorene

By: Muhammad Saifullah Bin Jumari (A0125182M)

Supervisor: Vitor Pereira

Department of Physics

National University of Singapore

A thesis submitted in
partial fulfillment of the requirements for the degree of
Bachelor of Science with Honours

Academic Year 2017/2018

This thesis is dedicated to my family and friends,
my pillars of strength.

Acknowledgements

Abstract

Phosphorene is well known for its superior mechanical flexibility and anisotropic structure which give rise to the remarkable tunability of its electronic properties. In particular, the high tunability of its optical gap could allow for the development of more versatile optoelectronic devices capable of manipulating light over a wider range of frequencies in the infra-red spectrum.

This work explores, for the first time, the sensitivity of the exciton binding energy in phosphorene to mechanical stress by combining the predictions of an effective model of excitons in 2D crystals with a tight-binding model which captures the effects of strain in phosphorene's band structure in the elastic regime.

From our results, we estimate that the exciton binding energy can be varied up to around 5% of its equilibrium value under 8% uniaxial strains in the elastic regime. Furthermore, we found that variations in the exciton binding energy contribute to about 20% of the total variation of the optical gap in these strain regimes. Overall, we see that the optical gap can be tuned in excess of 200 meV in this range, or by about 25 meV per 1% of uniaxial deformation. This extremely and unusually high sensitivity can be exploited in optoelectronic sensors.

Our findings and the future improvements of the models used could shed light on the key parameters which determine the strain sensitivity of the exciton spectrum in phosphorene. They also provide a gauge of the magnitude of strain tunability of the exciton binding energy in phosphorene which may serve as a guide for future work aiming to tackle this problem ab-initio.

Contents

Chapter 1

Introduction

It is said that sometimes, the hidden gems of the world lie just before us, waiting to be discovered. Indeed, while some scientific discoveries originate from a stroke of inspiration or imagination, such as Einstein's gedanken experiments, it is amusing to find that others are made via great serendipity or playfulness, with tools as rudimentary as sticky tape.

Such was the case with the unprecedented isolation of single layer graphene in 2004 by Novoselov and Geim, which led to the discovery of a host of other families of two-dimensional (2D) materials and propelled the field into its meteoric ascent [1]. The highly unusual properties of these materials as compared to conventional bulk 3D materials, coupled with the possibility of their practical realization, have sparked great interest within the scientific community in hopes of developing novel next-generation materials for advanced technological applications. On the theoretical front, 2D materials have been shown to display a wide multitude of unique properties with interesting correspondences with areas such as field theory and relativity, allowing theorists to draw inspiration across seemingly disparate areas in physics. The myriad of emergent properties exhibited by these 2D systems, characteristic of many-body interacting systems, allows for many fascinating aspects of these materials to be explored and developed for future uses.

1.1 Overview of two-dimensional (2D) materials

Two-dimensional materials are essentially crystals made of atoms arranged in 2D layers, with strong in-plane interatomic bonds holding the atoms in a planar structure. These crystals appear naturally in their bulk three-dimensional form, which consist of these 2D layers being stacked on top of each other, held together by weak inter-planar Van der Waals forces.

In their single-layer form, these materials are found to display remarkable properties. In the famous example of graphene, which is the 2D crystal which makes up the graphite in our pencils, the honeycomb structure of the carbon atoms gives rise to a Dirac cone in its band structure, which in turn results in an effective electronic dispersion in graphene akin to that of massless Dirac fermions [2]. This finding is truly remarkable from a theoretical standpoint since such behavior mimicking relativistic particles is unexpected.

From the point of view of semiconductor applications, these materials are poised for uses in various devices, owing to the wide range of band gap sizes across many classes of these materials. These band gaps range from 0 eV in graphene, ~ 2 eV in phosphorene to ~ 6 eV in hexagonal boron nitride (hBN) [3]. In transition metal dichalcogenides (TMDCs) for instance, the band gap of ~ 1.1 eV, similar to that of silicon, makes it highly suitable to be used in next-generation transistors [2]. The presence of an intrinsic direct band gap in many of these materials also gives rise to strong light-matter interactions, making them suitable for various optoelectronic applications [3].

Being two-dimensional in nature also endows these materials with characteristics which make them far more versatile and rich in nature as compared to conventional bulk 3D crystals. One important aspect is their reduced dimensionality, which leads to a greater exposure of the electrons in the material to the immediate surroundings and reduced dielectric screening of the electrons among themselves [4]. This makes them more **sensitive** to external conditions and perturbations such as mechanical stress or the presence of an external electric field. The application of stress, for instance, could give rise to more significant crystal deformations, which alters the electronic structure and band gaps of these materials. This sensitivity to external effects makes these materials more **tunable** than their 3D counterparts, which is a very useful and highly sought after property in technological applications. As such a degree of tunability is not easily replicated in conventional 3D crystals, it makes 2D materials far more versatile and potentially useful due to the possibility of implementing additional 'tuning knobs' to alter their behaviors in practical settings, on demand.

1.2   Anisotropy and tunability in phosphorene

If 2D materials were ranked based on their electronic and mechanical tunabilities, monolayer phosphorene will certainly lay claim to the top few positions. Phosphorene
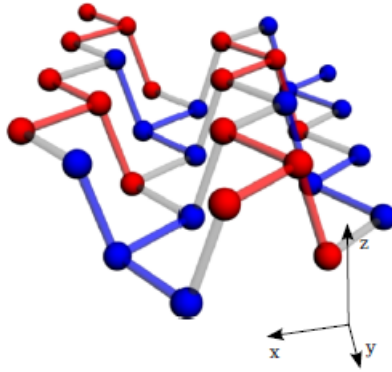
Figure 1.1: An illustration of the crystal structure of phosphorene [5]

is a 2D crystal consisting of purely phosphorous atoms. These atoms are arranged in a unique puckered arrangement due to the sp^3 hybridization of the valence 3s and 3p atomic orbitals of the valence electrons, giving rise to a bond angle of $\sim 103.69º$ [5]. Figure 1.1 shows the arrangement of the phosphorous atoms in phosphorene. Its crystal structure may be viewed as a tessellation of a unit consisting of four phosphorous atoms, highlighted in red and blue, which alternate throughout the structure and are related by a 180º rotation about the y axis.

The unique puckered structure in phosphorene makes it very susceptible to deformations under stress. The application of stress along phosphorene's armchair direction allows for a greater degree of deformation as compared to many other 2D materials because it is easier to straighten the bond angles associated with the armchair pucker as compared to increasing bond lengths between atoms. This makes phosphorene the only crystal capable of withstanding up to 30% structural deformation without breaking [6].
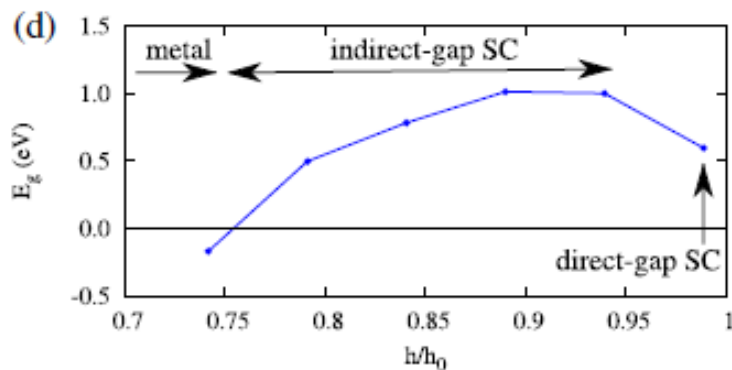
Figure 1.2: Strain-induced band gap modification in phosphorene calculated using density functional theory and tight-binding methods [5].

The structural flexibility of phosphorene consequently gives rise to a high tunability of its electronic properties and behavior. It has been shown, ab-initio, that a deformation of phosphorene in the z-direction can lead to very significant band gap changes. Figure 1.2 depicts the ab-initio calculated band gap of phosphorene under various compressional strain conditions, which clearly shows a semiconductor-metal transition in certain deformation regimes.

Apart from the puckering exhibited by the material, another unique feature is the inherent **anisotropy** in its crystal arrangement. The atomic arrangement of phosphorene repeats in a different way when moving along two orthogonal directions. Referring to Figure 1.1, moving along the x direction, one finds a puckered structure resulting in height variations in the z direction. The direction along which this pattern occurs is coined the 'armchair direction' in the literature. On the other hand, moving along the y direction, one observes a flat zig-zag-like structure of the phosphorous atoms, thus the term 'zigzag direction'. We shall henceforth interchangeably refer to the armchair and zigzag directions in phoshorene as the x and y directions respectively.

The different atomic arrangements along these two directions give rise to a host of various anisotropic properties i.e. those displaying dependence on the in-plane crystal direction. An important property is the asymmetry in its band structure near the Γ point. An ab-initio calculated band structure of phosphorene shown in the inset of Figure 1.3 demonstrates the different electronic dispersion along the ΓX (armchair) and ΓY (zigzag) directions [5]. This suggests that the electrons in phosphorene propagate with a significantly larger effective mass along the y direction as compared to the x direction due to the flatter energy dispersion curve along the ΓY direction.
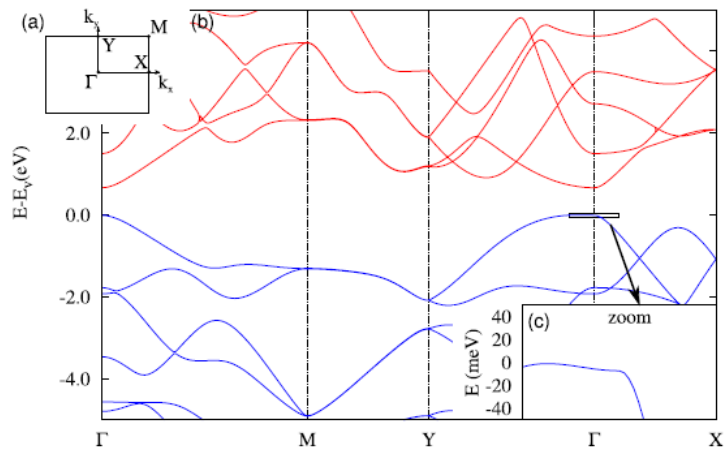
Figure 1.3: Band structure of phosphorene obtained from ab-initio methods [5]. The inset illustrates the anisotropic dispersion between the ΓX and ΓY directions.

In summary, phosphorene's flexibility coupled with its inherent structural anisotropy allows for a relatively large degree of freedom in the deformation of its crystal structure and consequently, the tunability of its electronic properties as compared to other 2D crystals. The existence of its armchair pucker makes it one of the most deformable materials in existence and gives rise to its large extent of tunability. In addition, the existence of its structural anisotropy allows for different ways of deformation depending on the **direction** of mechanical stress. This leads to an additional degree of freedom in deforming the material and tuning its properties, which is far less prominent in more isotropic materials such as graphene, thus making phosphorene potentially one of the most tunable 2D materials in existence.

1.3   Optical properties and excitons

The high tunability in phosphorene opens up opportunities to manipulate various properties of the material to a significant degree. Amongst those are its optical properties, which have been highlighted to play a potentially significant role in optoelectronic applications. As noted in [7, 4], the band gap in phosphorene sits nicely between the band gaps of TMDCs and graphene, which makes it act as a bridge in terms of band gap energies. Consequently, phosphorene fills the void in the range of the electromagnetic spectrum not covered by these 2D materials, as depicted in Figure 1.4. The existence of phosphorene therefore allows us to fill up various technological gaps and enables optoelectronic applications in frequency ranges which span the lower- to mid-infrared ranges in the electromagnetic spectrum that are previously unable to be accessed by the other 2D materials.
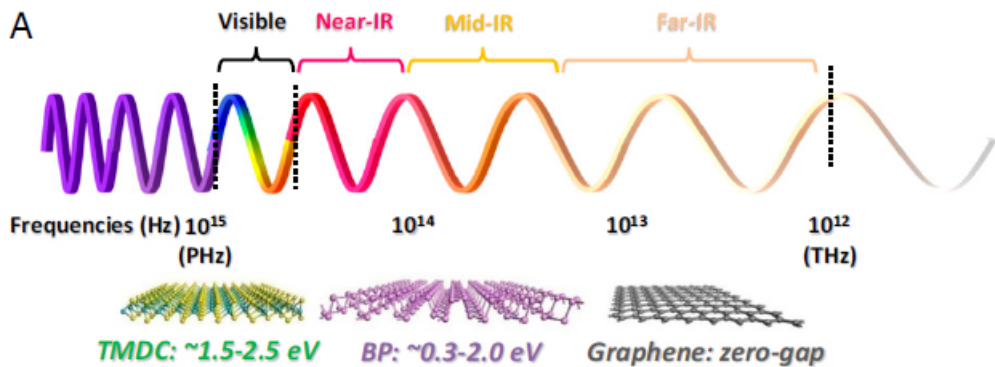
Figure 1.4: An illustration of various 2D materials and the range of the electromagnetic spectrum corresponding to their band gap sizes [7].

In optoelectronic applications, the optical gap of a material plays a crucial role because it determines the onset frequency at which the material absorbs light. As such, the ability to tune the optical gap is highly valuable, as it allows for novel optoelectronic components that are more tunable and receptive to light over a wider range of frequencies.

The optical gap is determined by two key factors, the band gap of the material and the ground state energy of an excitonic state in the material. An excitonic state, or exciton for short, is a bound state of an electron and hole pair which typically arises when an electron is excited from the valence band to the conduction band, leaving a hole in the valence band. As the hole can be regarded as a positively charged particle, the two may interact via the Coulomb interaction and can form bound states with specific energy levels, akin to that of the hydrogen atom [8]. These bound states have energies which typically lie below the conduction band as depicted in Figure 1.5.
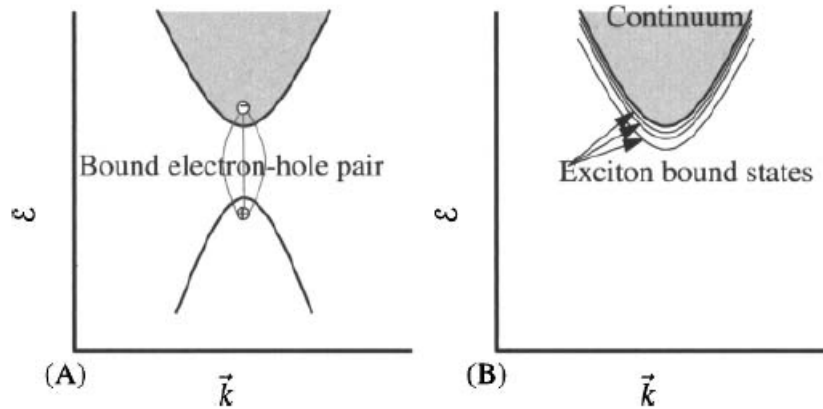
Figure 1.5: An illustration of an excitonic state as a bound electron-hole pair (left) and a depiction of excitonic energy levels beneath the conduction band (right) [9].

In the absence of an excitonic state, one expects a material to respond strongly only to light above a threshold frequency set by the band gap. This is because upon the impingement of light, an electron from the valence band is excited across the band gap into the conduction band. If excitons were included into the picture, the threshold frequency needed to excite an electron to a new state is now lower since the electron may now be excited from the top of the valence band to the ground exciton state, which lies below the conduction band. Thus, the threshold frequency at which light may be absorbed is given by the difference in the band gap size and the binding energy of the exciton. In principle, one would expect the absorption spectrum of a material to resemble the plot in Figure 1.6. In the absence of excitons, the onset

absorption frequency is set by the band gap ϵ_g as indicated by the dashed plot. In the presence of excitons however, absorption peaks are expected to appear at energies below ϵ_g, with offsets equal to the energy levels of the exciton spectrum as shown by the bold line. The sharpest peak occurs at an offset of the exciton binding energy R denoted in the diagram.
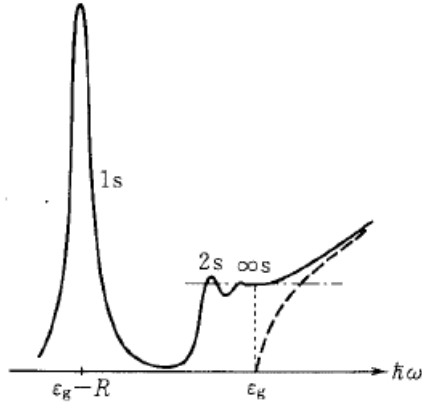
Figure 1.6: A schematic absorption spectrum depicting the situation with excitons (bold line) and without excitons (dashed lines) [8].

In conventional 3D bulk crystals, excitonic effects are relatively weak, with exciton binding energies of the order 1 meV, a thousand times smaller than the typical band gap size of the order 1 eV [10]. The optical gap and band gap are approximately equal in this case. However, in 2D crystals, the reduced dielectric screening among the electrons gives rise to much stronger excitonic effects, with exciton binding energies of the order 0.1 eV which is only 10 times smaller than the band gap size. As such, the difference between the optical and band gap sizes in 2D crystals are large enough to be picked up in photoluminescence or photoabsorption experiments and inevitably plays an important role in the optoelectronic applications of 2D materials [11].

1.4 Project overview

In light of the inherent structural flexibility displayed by phosphorene, there are many efforts to map the effect of mechanical stress to the electronic band structure of the material with ab-initio methods. On a separate front, there are also efforts to calculate the excitonic energy levels and wavefunctions ab-initio. However, possibly due to the huge amount of computational resources required, there have been no efforts to map the effect of stress to these exciton energy levels.

In our project, we explore the effect of uniaxial mechanical stress on the exciton binding energies in phosphorene by making use of two different effective models: the first being an effective model of excitons in 2D crystals and the second being a tight-binding model which allows us to predict the effect of stress on the band structure of phosphorene near the Γ point. We also examine the robustness of each effective model by comparing their predictions against ab-initio results in order to ascertain the reliability of our predictions.

By using effective models, we gain more clarity and understanding of the key parameters which determine the excitonic binding energies and the band structure of the material under stress. Such invaluable insight into the interplay between various properties of a system cannot be gleaned if one were to resort to full-blown ab-initio methods. Furthermore, even though these models are not highly accurate, they give reasonable estimates of the sensitivity of excitonic binding energies to stress. Therefore, their predictions can serve as a guide for future ab-initio calculations that handle the same problem in a more accurate and reliable manner.

The project report is arranged as follows: Chapter 2 gives a theoretical derivation of an effective Hamiltonian for excitons in 2D crystals which hinges strongly upon the use of an effective potential known as the Keldysh potential. Following that, Chapter 3 discusses the main methods we have adopted to compute the exciton energy levels from the model. Chapter 4 expounds upon the use of a tight-binding model and the interplay between stress and the geometry of the crystal before finally utilizing the results of the exciton model to obtain a relation between uniaxial stress and the exciton binding energies. We end off with some concluding remarks and possible future extensions of this project in Chapter 5.

Chapter 2

Theory: Effective model for excitons in 2D crystals

In order to predict the optical behavior of a 2D system, it is paramount to have a good model describing excitonic states in the system. The most reliable methods that are currently used to calculate the properties of these states involve full blown ab-initio calculations such as those involving the GW-Bethe-Salpeter equation, which takes into account many-electron interactions to compute excitonic wavefunctions and energies [12]. While these methods provide fairly reliable excitonic binding energies when compared to experimental values, ab-initio methods typically obscure the important parameters which enter the determination of certain properties of the system - in our case, excitonic states. As such, while these methods provide a good theoretical benchmark for important values, they do not provide insight into the key parameters which determine the behavior of these states.

One therefore looks for **effective** models which capture the key aspects and behavior of excitons where in this case, the fine details of the many-electron interactions are collectively manifest in the form of an effective interaction between the electron and hole pair. In doing so, we trade the accuracy arising from keeping track of every detail of the many-electron interaction in favor of deriving insight into the key effective parameters which enter into the properties of the excitonic states.

In this section, we shall, for the sake of completeness, first present an important derivation showing that excitonic states can be perceived as a bound state of an electron-hole pair under a suitable interaction potential, following the treatment from [8]. We then present the Keldysh potential, an effective potential which arises from charges interacting in a two-dimensional dielectric media. An effective Schrödinger for excitonic states in phosphorene is then presented towards the end.

2.1 Excitonic states

We consider a crystal and envision it as a rigid lattice of positively charged atomic nuclei with electrons bound to them via Coulomb interactions. We may write the Hamiltonian of this many-body system as

$$H = \sum_i \frac{P_i^2}{2m_e} + V_{lat}(\mathbf{r}_i) + \sum_{i \neq j} v(\mathbf{r}_i - \mathbf{r}_j). \tag{2.1}$$

The first term denotes the kinetic energy of the electrons, the second denotes the ion-electron interactions written in terms of a periodic lattice potential V_{lat} and the last term denotes the pairwise electron-electron interactions. We disregard the contribution of ion-ion interactions to the total energy of the system as it results in a constant energy shift since the ions are rigidly held in their places.

2.1.1 Second quantized representation

For a many body problem, it is more natural and convenient to work in the second quantized representation. As such, let us define creation and annihilation operators for position eigenstates of electrons $\Psi^\dagger(\mathbf{r}), \Psi(\mathbf{r})$ and a vacuum state $|0\rangle$ such that

$$\Psi^\dagger(\mathbf{r}) |0\rangle = |\mathbf{r}\rangle \tag{2.2}$$

where $|\mathbf{r}\rangle$ is a position eigenstate localized at position $\mathbf{r}$. The operators obey the anti-commutation relations for fermions,

$$\left\{\Psi(\mathbf{r}), \Psi^\dagger(\mathbf{r}')\right\} = \delta(\mathbf{r} - \mathbf{r}'), \qquad \left\{\Psi(\mathbf{r}), \Psi(\mathbf{r}')\right\} = 0. \tag{2.3}$$

Defining $h(\mathbf{r}, \mathbf{p}) = \frac{P^2}{2m} + V_{lat}(\mathbf{r})$, we may then write the Hamiltonian operator in this representation as

$$H = \int d\mathbf{r}\, \Psi^\dagger(\mathbf{r}) h(\mathbf{r}, \mathbf{p}) \Psi(\mathbf{r}) + \frac{1}{2} \int \int d\mathbf{r}\, d\mathbf{r}'\, \Psi^\dagger(\mathbf{r}) \Psi^\dagger(\mathbf{r}') v(\mathbf{r} - \mathbf{r}') \Psi(\mathbf{r}') \Psi(\mathbf{r}). \tag{2.4}$$

The first term corresponds to the kinetic and ion-electron interaction terms while the second corresponds to electron-electron interactions. For a rough interpretation of these terms, recall that $\Psi^\dagger(\mathbf{r})\Psi(\mathbf{r})$ is a number operator which counts the number of electron at location $\mathbf{r}$. The first term therefore counts on-site energies for each electron. Similarly, the second term counts the Coulomb interaction energy at two different sites, where the factor of $\frac{1}{2}$ accounts for the double-counting. For a full derivation of the operators in this representation, see [8].

2.1.2 Bloch and Wannier states

To aid in the derivation, let us recall that for a Hamiltonian operator H invariant under translation by any lattice vector $\mathbf{R}$ i.e. $[H, T_{\mathbf{R}}] = 0$, the eigenstates are Bloch states which take the form

$$\phi_{\nu\mathbf{k}}(\mathbf{r}) = e^{i\mathbf{k}\cdot\mathbf{r}} u_{\nu\mathbf{k}}(\mathbf{r}) \tag{2.5}$$

in the position basis, with the function $u_{\nu\mathbf{k}}(\mathbf{r})$ having a discrete symmetry corresponding to the lattice vector $\mathbf{R}$ i.e. $u_{\nu\mathbf{k}}(\mathbf{r}) = u_{\nu\mathbf{k}}(\mathbf{r} + \mathbf{R})$. The indices ν and $\mathbf{k}$ are the band index and wave vector respectively. We also remind ourselves that for a given band index ν, the wave vector $\mathbf{k}$ is not unique and that many $\mathbf{k}$, differing by a reciprocal lattice vector $\mathbf{G}$, correspond to the same state $\phi_{\nu\mathbf{k}}$. This is due to the fact that these Bloch states labelled by $\mathbf{k}$ satisfy the relation:

$$T_{\mathbf{R}} |\phi_{\nu\mathbf{k}}\rangle = e^{i\mathbf{k}\cdot\mathbf{R}} |\phi_{\nu\mathbf{k}}\rangle. \tag{2.6}$$

We find that for a given eigenvalue $e^{i\mathbf{k}\cdot\mathbf{R}}$, there exist multiple $\mathbf{k}$ which give rise to the same value. Specifically, states labelled by $\mathbf{k}$ and $\mathbf{k} + \mathbf{G}$ will equally fit the bill since $\mathbf{G} \cdot \mathbf{R} = 2\pi m$ where $m \in \mathbb{Z}$, recalling the general relation between lattice and reciprocal lattice vectors. As such, one need not look so far in $\mathbf{k}$-space to identify the various Bloch states due to this inherent periodicity. One is therefore comfortably restricted to the first Brillouin zone, which we denote 1BZ, where every $\mathbf{k}$ labels a unique Bloch state. In second quantization, we may define creation and annihilation operators $a^{\dagger}_{\nu\mathbf{k}}, a_{\nu\mathbf{k}}$ for a Bloch state in terms of $\Psi(\mathbf{r})$ as

$$a^{\dagger}_{\nu\mathbf{k}} = \int d\mathbf{r}\, \phi_{\nu\mathbf{k}}(\mathbf{r})\Psi^{\dagger}(\mathbf{r}) \tag{2.7}$$

with the corresponding expression for $a_{\nu\mathbf{k}}$ via Hermitian conjugation.

We also introduce the Wannier states, which are defined by a discrete Fourier transform of the Bloch states

$$\phi_{\nu n}(\mathbf{r}) = \phi_{\nu}(\mathbf{r} - \mathbf{R_n}) = \frac{1}{\sqrt{N}} \sum_{\mathbf{k} \in 1\text{BZ}} e^{-i\mathbf{k}\cdot\mathbf{R}_n} \phi_{\nu\mathbf{k}}(\mathbf{r}) \tag{2.8}$$

where N is the number of primitive cells in the crystal. In this transformation, the wave vector index $\mathbf{k}$ is exchanged for the site index n, reflecting the fact that these Wannier states are localized at site $\mathbf{R}_n$. We may also write the Wannier states in terms of creation and annihilation operators $a^{\dagger}_{\nu n}, a_{\nu n}$. The annihilation operators for Wannier states are related to those of the Bloch states by a Fourier transform

$$a_{\nu n} = \frac{1}{\sqrt{N}} \sum_{\mathbf{k}} e^{i\mathbf{k}\cdot\mathbf{R}_n} a_{\nu\mathbf{k}} \tag{2.9}$$

with the corresponding creation operators obtainable via a Hermitian conjugation and from here on, sums over $\mathbf{k}$ are assumed to be taken over the first Brillouin zone.

2.1.3 Single electron excitations

We begin by assuming that the ground state of the system consists of all the electrons occupying the Bloch states in the filled bands labelled by indices $\mu, \mathbf{k}$. We shall denote filled bands with the index μ and the empty bands with ν. As such, we write the ground state as

$$|g\rangle = \prod_{\mu\mathbf{k}} a_{\mu\mathbf{k}}^{\dagger} |0\rangle \tag{2.10}$$

where the indices run over the filled states.

Now lets consider the situation where an electron is excited from the Bloch state labelled by $(\mu, \mathbf{k})$ in the filled band to a state $(\nu, \mathbf{k} + \mathbf{K})$ in the empty band. This situation could arise when an electron absorbs a single photon of wave vector $\mathbf{K}$ with energy equal to the energy difference of the two Bloch states. Such a state is characterized by the quantum number $\mathbf{K}$ and is therefore an eigenstate of the Hamiltonian in (2.10) since it is invariant under lattice vector translations $T_{\mathbf{R}}$ [8]. Restricting ourselves to a fixed pair of bands μ, ν we see that there are multiple values of $\mathbf{k}$ which can give rise to such an eigenstate, i.e. there exists a degenerate subspace characterized by the quantum number $\mathbf{K}$. (We shall restrict ourselves to the subspace spanned by states with only one-electron excitations for simplicity). We can therefore write an eigenstate in this degenerate subspace as

$$|e\rangle = B^{\dagger} |g\rangle = \sum_{\mathbf{k}} f(\mathbf{k}) a_{\nu\mathbf{k}+\mathbf{K}}^{\dagger} a_{\mu\mathbf{k}} |g\rangle \tag{2.11}$$

$$= \frac{1}{N} \sum_{\mathbf{k}nn'} f(\mathbf{k}) e^{i\mathbf{k}\cdot(\mathbf{R}_n - \mathbf{R}_{n'})} e^{i\mathbf{K}\cdot\mathbf{R}_n} a_{\nu n}^{\dagger} a_{\mu n'} |g\rangle \tag{2.12}$$

$$= \frac{1}{\sqrt{N}} \sum_{nn'} F(\mathbf{R}_n - \mathbf{R}_{n'}) e^{i\mathbf{K}\cdot\mathbf{R}_n} a_{\nu n}^{\dagger} a_{\mu n'} |g\rangle \tag{2.13}$$

In deriving the final expression for this eigenstate, we have made used of (2.9) to convert from the Bloch to Wannier operators. We have also defined function F as the discrete inverse Fourier transform of f. The final expression is reminiscent of that of the composite wavefunction of an electron in band μ and a hole in band ν.

Specifically, we may interpret the term $e^{i\mathbf{K}\cdot\mathbf{R}_m}$ as analogous to a free particle wavefunction, and $F(\mathbf{R}_n - \mathbf{R}_{n'})$ as the wavefunction of the relative motion, suggesting that the electron-hole pair moves freely as a whole with wave vector $\mathbf{K}$, but are

bound together as described by the wavefunction F. One naturally seeks to obtain an effective Schrödinger equation for the wavefunction $F(\mathbf{r})$ for the relative motion of this bound pair, which allows for the calculation of its energy spectrum.

2.1.4 Effective exciton Schrödinger equation

An excitonic state is very well described by the state $|e\rangle$ above, since it is typically formed under excitation by absorbing a photon of fixed wave vector, giving rise to a bound state of an electron and a hole, as is strongly suggested by the form in (2.13). To obtain an equation which governs the excitonic wavefunction $f(\mathbf{k})$, we define a ground state energy E_g and an excited state energy E_e such that $H|g\rangle = E_g|g\rangle$ and $H|e\rangle = E_e|e\rangle = HB^\dagger|g\rangle$, where we used the relation $|e\rangle = B^\dagger|g\rangle$. Then it may be shown that

$$[H, B^\dagger] = (E_e - E_g)B^\dagger. \tag{2.14}$$

Then, reminding ourselves that $B^\dagger = \sum_\mathbf{k} f(\mathbf{k})a_{\nu\mathbf{k}+\mathbf{K}}^\dagger a_{\mu\mathbf{k}}$ from (2.11), we may extract $f(\mathbf{k})$ by first acting the equation above on $|g\rangle$ and then projecting the resulting equation onto the state $\langle g| a_{\mu\mathbf{k}}^\dagger a_{\nu\mathbf{k}+\mathbf{K}}$. In doing so, we see that the right-hand side reduces to $(E_e - E_g)f(\mathbf{k}) = Ef(\mathbf{k})$ where we let E be the excitation energy above the ground state energy. The full equation then reduces to an effective Schrödinger equation governing a momentum space wavefunction $f(\mathbf{k})$

$$\sum_\mathbf{k} H_{\mathbf{k}'\mathbf{k}} f(\mathbf{k}) = Ef(\mathbf{k}') \tag{2.15}$$

where the matrix elements $H_{\mathbf{k}'\mathbf{k}}$ are given by

$$H_{\mathbf{k}'\mathbf{k}} = \langle g| a_{\mu\mathbf{k}'}^\dagger a_{\nu\mathbf{k}'+\mathbf{K}}[H, a_{\nu\mathbf{k}+\mathbf{K}}^\dagger a_{\mu\mathbf{k}}] |g\rangle. \tag{2.16}$$

We shall skip the cumbersome process of evaluating these matrix elements since they are beyond the scope of this project. Ultimately, one may show that the matrix elements take on the form

$$H_{\mathbf{k}'\mathbf{k}} = \delta_{\mathbf{k}'\mathbf{k}}\left[\epsilon_\nu(\mathbf{k}+\mathbf{K}) - \epsilon_\mu(\mathbf{k})\right] - v_{\nu\mathbf{k}'+\mathbf{K}\,\mu\mathbf{k}\,\mu\mathbf{k}'\,\nu\mathbf{k}+\mathbf{K}} + v_{\mu\mathbf{k}\,\nu\mathbf{k}'+\mathbf{K}\,\mu\mathbf{k}'\,\nu\mathbf{k}+\mathbf{K}} \tag{2.17}$$

where $\epsilon_\mu(\mathbf{k})$ denotes the eigenvalues corresponding to the Hartree-Fock states, $\phi_{\nu\mathbf{k}}$, and the last two terms are matrix elements of the interaction term $v(\mathbf{r} - \mathbf{r}')$ in the Hartree-Fock basis i.e. corresponding to the states. In brief, the Hartree-Fock states are the solutions to the self-consistent Hartree-Fock equations, which approximates

the many-body wavefunction of a system with a single Slater determinant [8]. As the details of the Hartree-Fock method lie beyond the scope of the project, we will not delve into the details here but simply note that it is a technique used to approximate the energy eigenstates and eigenvalues of a many-body system.

Physically, the matrix elements may be understood as follows - the Kronecker delta term gives a band gap contribution to the total energy, since ν and μ correspond to the valence and conduction bands respectively for the case of excitons. That this term is diagonal in $\mathbf{k}$ suggests that it is purely kinetic. It is the energy needed to excite an electron from the valence to conduction band without any interaction between the electron and hole. The last two terms arise due to the Coulomb interaction between the electron-hole pair. The interaction term with the negative sign gives rise to an attractive interaction, expected of Couloumb forces between opposite charges while the term with the positive sign correspond to exchange correlation contributions.

To obtain a more familiar Schrödinger equation in real space, one switches to the Wannier basis by using the relation (2.8), which amounts to a Fourier transform

$$H_{ll'} = \frac{1}{N} \sum_{\mathbf{k}\mathbf{k}'} e^{i\mathbf{k}'\cdot\mathbf{R}_l} H_{\mathbf{k}'\mathbf{k}} e^{-i\mathbf{k}\cdot\mathbf{R}_{l'}} \tag{2.18}$$

and leads to the relation

$$\sum_{l'} H_{ll'} F(\mathbf{R}_{l'}) = E F(\mathbf{R}_l). \tag{2.19}$$

Assuming that the Wannier states are well-localized about $\mathbf{R}_l$, one may use suitable approximations to show that the last two interaction terms in (2.17) reduce to

$$-\delta_{ll'} v(\mathbf{R}_l) + \delta_{l0}\delta_{l'0} w_{\mathbf{K}} \tag{2.20}$$

where the first term is the familiar interaction potential at $\mathbf{R}_l$ centered at the origin [8]. The second term is due to exchange correlations and can be shown to take the form

$$w_{\mathbf{K}} = \sum_{m} e^{-i\mathbf{K}\cdot\mathbf{R}_m} w(\mathbf{R}_m) \tag{2.21}$$

with

$$w(\mathbf{R}_1 - \mathbf{R}_2) = \int\int d\mathbf{r} \, d\mathbf{r}' \, \phi_\nu^*(\mathbf{r} - \mathbf{R}_1)\phi_\mu(\mathbf{r} - \mathbf{R}_1) v(\mathbf{r} - \mathbf{r}')\phi_\mu^*(\mathbf{r} - \mathbf{R}_2)\phi_\nu(\mathbf{r} - \mathbf{R}_2). \tag{2.22}$$

On the other hand, the band gap term in (2.16) becomes, in the position basis,

$$\frac{1}{N} \sum_{\mathbf{k}} e^{i\mathbf{k}\cdot(\mathbf{R}_l - \mathbf{R}_{l'})} \epsilon_\nu(\mathbf{k}) = E_\nu(\mathbf{R}_l - \mathbf{R}_{l'}). \tag{2.23}$$

Acting this on the real space wavefunction F in (2.19), we arrive at

$$\sum_{l'} E_\nu(\mathbf{R}_l - \mathbf{R}_{l'}) F(\mathbf{R}_{l'}) = \sum_m E_\nu(\mathbf{R}_m) F(\mathbf{R}_l - \mathbf{R}_m) \tag{2.24}$$

$$= \sum_m E_\nu(\mathbf{R}_m) e^{-i\mathbf{R}_m \cdot \nabla_l} F(\mathbf{R}_l) \tag{2.25}$$

$$= \epsilon_\nu(-i\nabla_l) F(\mathbf{R}_l) \tag{2.26}$$

where ϵ now explicitly takes the form of a differential operator acting of the wavefunction, allowing us to do away with the summation.

Collecting the terms, the real-space matrix elements read

$$H_{ll'} = \delta_{ll'} \left[\epsilon_\nu(-i\nabla_l + \mathbf{K}) - \epsilon_\mu(-i\nabla_l) - v(\mathbf{R}_l) \right] + \delta_{l0}\delta_{l'0} w_{\mathbf{K}}. \tag{2.27}$$

Three final simplifications may be made here. First, an exciton typically arises via photon absorption. For a photon with typical energy scale of the order of the band gap size 1 eV, this amounts to a photon wavelength of over a few thousand angstroms i.e. thousands of lattice spacings apart in the crystal as one may check with the relation $\lambda = hc/E$. Thus, the photon wavelength corresponds to momentum scales which are insignificant as compared to the momentum scales characteristic to Bloch state (which correspond to length scales of the order of a lattice spacing). This therefore allows us to neglect the wavevector $\mathbf{K}$ in (2.27).

Second, we are considering the specific case of a **Wannier-Mott exciton**, which involves a long-range interaction between an electron and hole pair at distances of the order of $\gtrsim 20$ lattice spacings. As such, we expect the wavefunction $F(\mathbf{r})$ to be slowly varying over length scales of lattice spacings and we may neglect terms which arise from higher derivatives of F such as $\nabla^3 F$ and above. This allows us to Taylor expand ϵ_μ and only keep terms up to second order. Expanding about the extrema at $\mathbf{k} = 0$ explicitly,

$$\epsilon_\nu(\mathbf{k}) - \epsilon_\mu(\mathbf{k}) = E_g + \sum_{ij} \frac{\hbar^2}{2m_{ij}} k_i k_j + O(k^3) \tag{2.28}$$

where $E_g = \epsilon_\nu(0) - \epsilon_\mu(0)$ is the band gap and the coefficients m_{ij} form the effective mass tensor. In position space, one makes the replacement $\mathbf{k} \to -i\nabla$ after doing this expansion.

Finally, the final term in (2.27) can be shown to be negligible. For a Coulomb interaction, the expectation value of this term in the 1s Hydrogen state of Bohr radius a goes as $\left(\frac{d}{a}\right)^3$, where d is a lattice spacing [8]. Thus, for the length scales of the exciton we are considering, where $a >> d$, we expect the exchange correlation term to contribute negligibly. We may finally write the full effective excitonic Schrödinger equation as

$$\left[-\sum_{ij} \frac{\hbar^2}{2m_{ij}} \nabla_i \nabla_j - v(\mathbf{r})\right] \psi(\mathbf{r}) = E\psi(\mathbf{r}) \tag{2.29}$$

where we have replaced F with the more familiar symbol for the real space wavefunction ψ and we made the replacement $E - E_g \to E$ in the final expression. In suitable coordinates, the effective mass tensor may be diagonalized. As such, the exciton may be regarded as analogous to a hydrogen atom with different effective masses along each direction.

2.2 The Keldysh potential

The derivation of the effective exciton Schrödinger equation presented previously leaves the pairwise interaction term $v(\mathbf{r})$ unspecified. In bulk 3D crystals, this interaction is the screened Coulomb interaction $\frac{e^2}{\kappa r}$, with dielectric constant κ, where we work in cgs units. However in 2D crystals, the electrons now interact in a 2D plane instead and experience less dielectric screening as compared to their 3D counterparts, with a rather different geometry. We therefore expect the effective electrostatic interaction between charges in this two-dimensional dielectric environment to take on a different form. In this section, we demonstrate that the electrostatic potential between charges in a 2D dielectric media may be described by the Keldysh potential, which is crucial in describing the behavior of excitonic states in 2D crystals.

2.2.1 Electrostatics in 2D media

We shall consider the electric potential generated by a perfect two-dimensional dielectric layer of zero thickness in response to the presence of an electric charge [13, 14]. To make the model more realistic, the layer shall also be envisioned to be placed on a dielectric slab with dielectric constant ϵ.

Using Cartesian coordinates, with z axis illustrated in Figure 2.1 and $x - y$ axis in-plane, let us position this layer on the plane $z = h$, at a height h above the dielectric slab present throughout the region $z < 0$. If a point charge q were placed
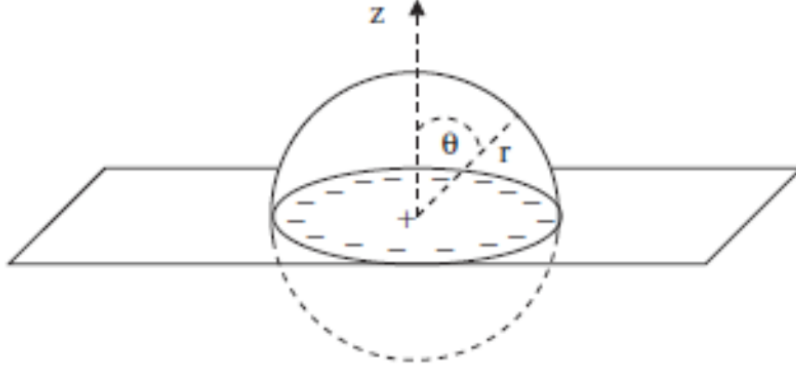
Figure 2.1: Illustration of charge distribution induced in a 2D dielectric media by an in-plane positive point charge [13]

at $\mathbf{r_0} = (0, 0, h)$ i.e. at the same plane as the 2D layer, the Poisson's equation for electrostatics $\nabla^2 \Phi = -4\pi\rho$ suggests that the electrostatic potential generated from this configuration of charges satisfies the relation

$$-\frac{1}{4\pi}\nabla^2\Phi = q\delta^3(\mathbf{r} - \mathbf{r_0}) + \delta(z - h)\sigma_L(s) + \delta(z)\sigma_B(s)$$

with the variables $\mathbf{r} = (x, y, z)^T$ and $\mathbf{s} = (x, y)^T$. On the right hand side of the equation, the first term corresponds to the point charge q, the second refers to the induced surface charge within the 2D layer (denoted by L) and the third term refers to the induced surface charge of the bulk dielectric (denoted by B) [14]. Note that due to the azimuthal symmetry of the system, the induced charges in the 2D plane and the bulk dielectric have distributions which only depend on the in-plane distance s from the origin.

Working in Fourier space proves to provide an expedient way to obtain the in-plane interaction potential. As such, we take the Fourier transform of the equation to obtain

$$\frac{1}{4\pi}(p^2 + k^2)\hat{\Phi} = \frac{1}{\sqrt{2\pi}}\left[\frac{q}{2\pi} + \tilde{\sigma}_L(p)\right]e^{-ihk} + \frac{1}{\sqrt{2\pi}}\tilde{\sigma}_B(p), \qquad (2.30)$$

where the tilde denotes the in-plane Fourier transform corresponding to the vector $\mathbf{s}$. The new quantities $\mathbf{p}$ and $\mathbf{k}$ are the wave vectors corresponding to the in-plane and normal directions respectively. As the next step, we proceed to obtain an expression which relates $\tilde{\sigma}_B$ to $\tilde{\sigma}_L$. Begin with the proportionality between the polarization of the bulk dielectric and the total electric field,

$$\mathbf{P}_B = \chi\mathbf{E} \qquad (2.31)$$

17

and use the fact that the surface charge on the bulk dielectric at $z = 0$ is equal to the normal component of the polarizability, $P_{B,z}$

$$\sigma_B(s) = \mathbf{P}_B \cdot \hat{\mathbf{n}}|_{z=0} = P_{B,z}(s, z = 0). \tag{2.32}$$

These give rise to

$$\sigma_B(s) = \chi E_z(s, z = 0). \tag{2.33}$$

At this stage, we note that the total field can be written in terms of the contribution by the induced charges on the bulk dielectric, $\mathbf{E}_B$ and the other charges i.e the point charge and the induced charges on the 2D layer which we collectively denote $\mathbf{E}_{\text{others}}$,

$$\mathbf{E} = \mathbf{E}_B + \mathbf{E}_{\text{others}}. \tag{2.34}$$

Now consider Gauss' law $\nabla \cdot \mathbf{D} = \rho_f$ near the surface of the bulk dielectric. Since there are no free charges there, we may set $\rho_f = 0$. Applying Gauss's theorem to this relation near the local vicinity of the surface, we find that

$$D_{z,\text{above}} = D_{z,\text{below}} \tag{2.35}$$

where 'above' and 'below' refer to a vicinity infinitesimally above and below the surface. Now invoking $\mathbf{D} = \frac{1}{4\pi}\mathbf{E} + \mathbf{P} = \frac{1}{4\pi}(1 + 4\pi\chi)\mathbf{E}$ and noting that there are no charges immediately above the surface, the relation implies

$$E_z(z = \epsilon) = (1 + 4\pi\chi)E_z(z = -\epsilon) \tag{2.36}$$

where ϵ is an infinitesimal value. Then, we use (2.34) and the fact that near the local vicinity of the surface, $|E_{B,z}(s)| = 2\pi\sigma_B(s)$, as the relation for an infinite plane of constant charge holds true for a plane with varying charge distribution but only locally. Taylor expanding about $z = 0$ and taking the limit $\epsilon \to 0$, this leads to

$$2\pi\sigma_B + E_{\text{others,z}} = (1 + 4\pi\chi)(-2\pi\sigma_B + E_{\text{others,z}}). \tag{2.37}$$

where the relation holds true only for $z = 0$. After some manipulation, this leads to the relation

$$\sigma_B(s) = \frac{\chi}{1 + 2\pi\chi}E_{\text{others,z}}(s, z = 0). \tag{2.38}$$

Taking this further and applying Coulomb's law on the right hand side, this gives

$$\sigma_B(s) = \frac{\chi}{1 + 2\pi\chi} E_{\text{others},z}(s) \tag{2.39}$$

$$= -\frac{\chi}{1 + 2\pi\chi} \int_{z=h} \left[q\delta^2(s') + \sigma_L(s') \right] \frac{h}{[h^2 + (s' - s)^2]^{3/2}} \, d^2s' \tag{2.40}$$

$$= -\frac{\chi}{1 + 2\pi\chi} \left[q\delta^2(s) + \sigma_L(s) \right] * \frac{h}{[h^2 + s^2]^{3/2}}, \tag{2.41}$$

where in the final line, we write the integral as a convolution of two functions for ease of performing a Fourier transform. We remind that the point charge and the 2D plane lies on the plane $z = h$ and the bulk surface charges lie below them at $z = 0$, hence the minus sign. Now, using the convolution theorem (i.e. if $h = f * g$, then $\tilde{h} = \tilde{f}\,\tilde{g}$) and using the identity

$$\mathscr{F}_s \left[\frac{h}{(h^2 + s^2)^{3/2}} \right] = 2\pi e^{-hp}, \tag{2.42}$$

where the operator $\mathscr{F}_s$ denotes a planar Fourier transform, we may obtain an expression for $\tilde{\sigma}_B(p)$

$$\tilde{\sigma}_B(p) = -\frac{2\pi\chi}{1 + 2\pi\chi} \left[\frac{q}{2\pi} + \tilde{\sigma}_L(s) \right] e^{-hp}. \tag{2.43}$$

Now, we obtain a relation between $\hat{\Phi}$ and $\tilde{\sigma}_L$. Begin with the polarization of the 2D layer, $\mathbf{P}(s) = -\xi\nabla_s\Phi(s, z = h)$ where ξ is the polarizability, and $\sigma_L = -\nabla \cdot \mathbf{P}$. Here, we have assumed that the polarizability tensor of the 2D material is diagonal. This implies

$$\sigma_L = \xi\nabla_s^2\Phi(s, z = h) = \xi\nabla_s^2\Phi_{2D}(s). \tag{2.44}$$

Here we define the potential within the plane as $\Phi_{2D}(s)$. Performing an in-plane Fourier transform on this equation and casting the result in terms of the full Fourier transform,

$$\tilde{\sigma}_L(p) = -\xi p^2 \int \frac{1}{\sqrt{2\pi}} \hat{\Phi}(p, k) e^{ihk} \, dk = -\xi p^2 \tilde{\Phi}_{2D}(p). \tag{2.45}$$

Now inserting $\hat{\Phi}(p, k)$ from (2.30) into the above relation, eliminating $\tilde{\sigma}_B$ using (2.43) and taking the limit $h \to 0$, it may be shown after several lines of calculation that the equation above reduces to

$$\tilde{\sigma}_L(p) = -\frac{2\pi\xi p}{1 + 2\pi\chi} \left[\frac{q}{2\pi} + \tilde{\sigma}_L(p) \right], \tag{2.46}$$

which gives the expression

$$\tilde{\sigma}_L(p) = -\frac{q\xi p}{1 + 2\pi\chi + 2\pi\xi p}.$$

(2.47)

Defining the average dielectric constant $\kappa = \frac{1+\epsilon}{2} = 1+2\pi\chi$ and a characteristic length scale $r_0 = \frac{2\pi\xi}{\kappa}$ and using (2.45) to exchange $\tilde{\sigma}_L(p)$ for $\tilde{\Phi}_{2D}(p)$, we obtain the Fourier transform of the induced potential in the 2D layer:

$$\tilde{\Phi}_{2D}(p) = \frac{q}{\kappa p(1 + r_0 p)}.$$

(2.48)

Taking the inverse Fourier transform [14], we obtain the Keldysh potential,

$$\Phi_{2D}(r) = \frac{q}{\kappa r_0}\frac{\pi}{2}\left[H_0\left(\frac{r}{r_0}\right) - Y_0\left(\frac{r}{r_0}\right)\right]$$

where r is now the in-plane distance, $H_0(x)$ is the zeroth order Struve function and $Y_0(x)$ is the zeroth order Bessel function of the second kind.
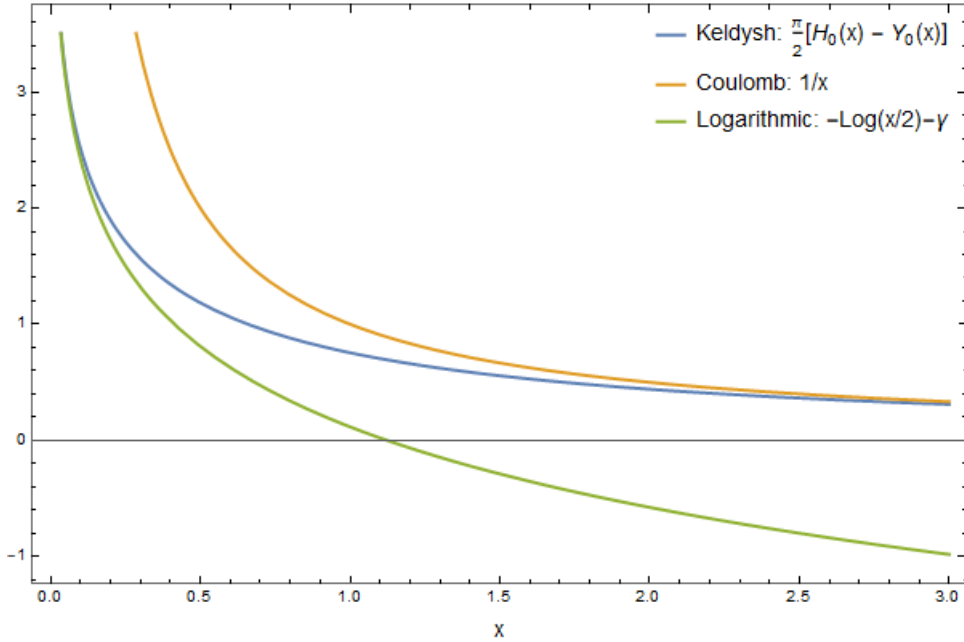

Figure 2.2: Plot of the Keldysh Potential and its limiting behaviors.

2.2.2 Characteristics of the Keldysh potential

The Keldysh potential exhibits a specific asymptotic behaviour in regimes set by the characteristic length scale, r_0. We remind that $r_0 = \frac{2\pi\xi}{\kappa}$, proportional to the polarizability of the 2D media and inverse to the dielectric screening.

Consider the case where the bulk dielectric is removed and the 2D layer is suspended in vacuum, then one takes the $\xi \to 0$ limit and expects to recover the Coulomb behavior. Let us write the potential in terms of

$$U(x) = \frac{\pi}{2}\left[H_0\left(x\right) - Y_0\left(x\right)\right] \tag{2.49}$$

i.e. $\Phi_{2\mathrm{D}}(r) = \frac{q}{\kappa r_0}U(\frac{r}{r_0})$. In the limit $r >> r_0$, which corresponds to the limit $x \to \infty$, $U(x) \sim \frac{1}{x}$. This therefore implies

$$\lim_{r/r_0 \to \infty} \Phi_{2D}(r) = \frac{q}{\kappa r} \tag{2.50}$$

which is precisely the Coulomb behavior. This also means that at very large distance scales, charges within the 2D plane interact as if they were in 3D media.

Something more intriguing occurs in the opposite limit $r << r_0$. This corresponds to the case of a very polarizable object i.e. the electrons freely redistribute themselves like in a metal. In this limit where $x \to \infty$, $U(x) \sim -\left(\ln\frac{x}{2} + \gamma\right)$ where $\gamma = 0.57721$ is the Euler-Mascheroni constant. The potential then behaves as

$$\lim_{r/r_0 \to 0} \Phi_{2D}(r) = -\frac{q}{\kappa r_0}\left(\ln\frac{r}{2r_0} + \gamma\right). \tag{2.51}$$

We observe that in this limit, the singularity at $r = 0$ is of a logarithmic nature and not that of a simple pole as in the case of the Coulomb interaction. This is reminiscent of the electrostatic behavior of an infinite charged rod, which can be shown using the equations above but are beyond the scope of the project. The Keldysh potential therefore interpolates between logarithmic behavior and the inverse Coulomb behavior across the entire domain, $x \in \mathbb{R}^+$. This illustrated in Figure 2.2. We find that in 2D media, the effective interaction between charges is stronger than that of 3D media as suggested by the plot.

In deriving the Keldysh potential, we have made use of several assumptions that one should be aware of:

1. The 2D layer is sandwiched between vacuum and a bulk dielectric

2. The polarizability tensor of the 2D plane is diagonal

3. The 2D plane has zero thickness

The first assumption gives rise to the average dielectric constant $\kappa = \frac{1+\epsilon}{2}$ where ϵ is the dielectric constant of the bulk dielectric, which plays the role of a substrate. However, one may proceed to do an alternative derivation, replacing the vacuum

with a second bulk dielectric lying above the layer, in order to show using similar methods that the notion of the average dielectric constant is preserved. In that more general case, the average dielectric constant becomes $\kappa = \frac{\epsilon_1 + \epsilon_2}{2}$ where ϵ_1 and ϵ_2 are the dielectric constant of the dielectric material above and below the 2D layer respectively.

The other assumptions are required to attain an exact analytic expression for the potential. Relaxing these assumptions makes it far more difficult perform the inverse Fourier transform and obtain the expression for the potential. Therefore, there are several clear drawbacks arising from these assumptions; first, the information on the anisotropy of the polarizability of the crystal is lost since we have assumed that its polarizability tensor is diagonal. This gives rise to an isotropic Keldysh potential, which ignores such features. Nonetheless, if the anisotropy involved is negligible, this serves as a good approximation.

On the other hand, in modelling the crystal as a 2D layer with zero thickness, we lose the subtle 3D nature of the crystal. However, we note that introducing the notion of a height in 2D crystals is rather subtle since it is not well defined - the electron cloud which permeates the crystal does not give a sharp boundary for one to define a height in a straightforward manner.

Despite the various drawbacks of the model potential, the key ingredient captured using this approach is the two-dimensional nature of medium. This captures the crucial aspect of how the dielectric screening between charges in 2D crystals significantly departs from that of the usual Coulomb interaction in 3D crystals and we may see that this arguably plays a major role in determining the magnitude of the excitonic binding energy.

2.3 Effective exciton Hamiltonian in 2D crystals

Combining the ideas from sections 2.1 and 2.2, we arrive at a picture of an exciton in 2D crystal as that of a bound state of an electron and hole interacting via the Keldysh potential. We can therefore write the Hamiltonian of the exciton in a generic 2D crystal as such:

$$H_{ex} = -\frac{\hbar^2}{2\bar{\mu}_x}\frac{\partial^2}{\partial x^2} - \frac{\hbar^2}{2\bar{\mu}_y}\frac{\partial^2}{\partial y^2} - \frac{e^2}{\kappa r_0}\frac{\pi}{2}\left[H_0\left(\frac{r}{r_0}\right) - Y_0\left(\frac{r}{r_0}\right)\right] \qquad (2.52)$$

with $r = \sqrt{x^2 + y^2}$.

The key parameters which enter the Hamiltonian are the effective masses along each direction $\bar{\mu}_{x/y}$, the polarizability ξ of the 2D crystal and the average dielectric

constant of the environment κ (via $r_0 = 2\pi\xi/\kappa$) which is dependant on the choice of substrate and the environment above the 2D layer.

The effective masses are comprised of the effective masses of the electron and hole along each direction, $m_{x/y}^{e/h}$. Written explicitly,

$$\bar{\mu}_{x/y} = \frac{m_{x/y}^e m_{x/y}^h}{m_{x/y}^e + m_{x/y}^h}. \tag{2.53}$$

The average dielectric constant is given by

$$\kappa = \frac{\epsilon_1 + \epsilon_2}{2} \tag{2.54}$$

where ϵ_1 is the dielectric constant of the medium above the 2D crystal while ϵ_2 is that of the substrate on which the crystal is placed. We note that the presence of anisotropic masses in (2.52) which breaks the azimuthal symmetry about the z-axis makes it impossible to decompose the effective Schrödinger equation into angular and radial equations, as in the case of the hydrogen atom. Furthermore, the presence of the Keldysh potential also does not allow for an exact analytic solution of the eigenstates and energies of the Hamiltonian. This necessitates the need for numerical methods to obtain the excitonic binding energies from the model.

2.3.1 Anisotropic coordinates

To gain an alternative interpretation of the Hamiltonian and also simplify the subsequent process of numerical calculations slightly, we introduce anisotropic coordinates in order to induce an ordinary Laplacian term in (2.52). This specifically involves performing the following coordinate transformation

$$x \to \sqrt{\frac{2\bar{\mu}}{\bar{\mu}_x}}x, \quad y \to \sqrt{\frac{2\bar{\mu}}{\bar{\mu}_y}}y \tag{2.55}$$

where $\bar{\mu} = \frac{\bar{\mu}_x \bar{\mu}_y}{\bar{\mu}_x + \bar{\mu}_y}$. Upon doing so, the derivatives turn into a Laplacian term, $-\frac{\hbar^2}{4\bar{\mu}}\nabla^2_{(x,y)}$ whereas the radial coordinate, r turns into $\sqrt{(1+\beta)x^2 + (1-\beta)y^2}$ where we introduce an **anisotropy parameter** β defined as

$$\beta = \frac{\mu_y - \mu_x}{\mu_y + \mu_x}. \tag{2.56}$$

From this point onwards, we introduce the effective masses without the overbars as defined by

$$\mu_{x/y} = \frac{\bar{\mu}_{x/y}}{m_e}, \quad \mu = \frac{\bar{\mu}}{m_e} = \frac{\mu_x \mu_y}{\mu_x + \mu_y} \tag{2.57}$$

23

where m_e is the electron mass. If we denote the original Keldysh potential as $\frac{e^2}{\kappa r_0}U(r')$ for cogency, where

$$U(r') = \frac{\pi}{2}[H_0(r') - Y_0(r')] \tag{2.58}$$

and $r' = \sqrt{(1+\beta)x^2 + (1-\beta)y^2}$, we may write the Hamiltonian in this coordinates as

$$H_{ex} = -\frac{\hbar^2}{4\mu m_e}\nabla^2_{(x,y)} - \frac{e^2}{\kappa r_0}U(\sqrt{(1+\beta)x^2 + (1-\beta)y^2}). \tag{2.59}$$

In doing so, we shift the anisotropy of the effective masses to the originally isotropic potential, inducing an effective anisotropic potential. In this picture, we may make some preliminary observations. As the parameter $\beta \in [0,1)$, where β close to unity implies very high anisotropy, we see that for the case where the effective mass along y is much larger than that along x i.e. $\mu_y >> \mu_x$, the coefficient for the y^2 term in the argument of the effective potential will be far smaller than the coefficient of the x^2 term. From a more geometric perspective, this means that the potential in anisotropic coordinates may be described by elliptical equipotential lines which are elongated along y and compressed along x for $\beta > 0$ as compared to circular lines in ordinary coordinates.

2.3.2 Dimensionless exciton Hamiltonian

To further aid the process of solving for the eigenvalues and eigenstates of the Hamiltonian, we shall rewrite the Hamiltonian further in a more convenient form. Let us set the anisotropy parameter $\beta = 0$ for simplicity as it only appears in the argument of the Keldysh potential and is dimensionless. We first write the Hamiltonian as a product of a scalar quantity with dimensions of energy and an operator which is dimensionless, following the treatment in [14]. The starting point would be to rewrite the coordinates in terms of the length scale r_0. To do this, we pull an overall factor out of the Hamiltonian and induce a coefficient r_0^2 for the Laplacian operator. This leads to

$$H_{ex} = -\frac{\hbar^2}{4\mu m_e r_0^2}\left[r_0^2\nabla^2 + \frac{4\mu m_e r_0 e^2}{\kappa\hbar^2}U\left(\frac{r}{r_0}\right)\right]. \tag{2.60}$$

Now we let $z = r/r_0$, a dimensionless length scale. We define the dimensionless quantity G given by

$$G = \frac{4\mu r_0 m_e e^2}{\kappa\hbar^2} = \frac{4\mu r_0}{\kappa a_0}, \tag{2.61}$$

24

which may be interpreted as the coupling strength between the electron and hole. Here, we have introduced the Bohr radius $a_0 = \frac{\hbar^2}{m_e e^2}$. Lastly, we may write the factor outside the square brackets in terms of the Hartree energy, $1\text{Ha} = \frac{\hbar^2}{m_e a_0^2}$

$$\frac{\hbar^2}{4\mu m_e r_0^2} = \frac{1\text{Ha}}{GW} \tag{2.62}$$

where the quantity W is given by

$$W = \frac{\kappa r_0}{a_0}. \tag{2.63}$$

The Hamiltonian in dimensionless coordinates, x may therefore be written

$$H_{ex} = -\frac{1\text{Ha}}{GW} \left[\nabla_z^2 + GU(z) \right] = -\frac{1\text{Ha}}{GW} \mathscr{H}. \tag{2.64}$$

Note that the parameters G, W and the operator $\mathscr{H}$ are dimensionless. We may therefore focus on solving for the eigenvalues and eigenvectors of the dimensionless Hamiltonian $\mathscr{H}$ and re-scale the problem accordingly.

Chapter 3

Computation: Exciton energy spectrum

We are interested in using the effective exciton Hamiltonian presented previously to obtain the energy spectrum and eigenstates of excitons in phosphorene. Based on the model, the main parameters which determine the exciton energy spectrum are μ (effective mass of the electron-hole pair), β (anisotropy parameter), ξ (in-plane polarizability of phosphorene) and κ (average dielectric constant of the environment). As the primary objective of the project is to ascertain how sensitive the excitonic binding energies are to the application of strain, the key parameters which would be altered under strain are strictly μ, β and ξ. However, in this project, we shall neglect the effect of changes in ξ under strain as a first approximation. As such, the main objective of the computation would be to obtain a set of values which provide a map $(\mu, \beta) \to E$ where E denotes an eigenvalue of the Hamiltonian.

In this section, we present the main methods we used to compute the exciton spectrum using the effective Hamiltonian. We then demonstrate the robustness of our method of computation by performing a consistency check against the paper which suggested the model [14]. The predictions of this model are then compared to exciton energies and wavefunctions in other papers in the literature to ascertain the degree to which it is reliable.

3.1 Eigenvalue problem solving

The primary objective is to find the solution to the following eigenvalue problem

$$-\frac{1\text{Ha}}{GW} \left[\nabla^2_{(x,y)} + GU(\sqrt{(1+\beta)x^2 + (1-\beta)y^2}) \right] \psi(x,y) = E\psi(x,y) \qquad (3.1)$$

where

$$U(z) = \frac{\pi}{2} \left[H_0(z) - Y_0(z) \right] \tag{3.2}$$

and $G = \frac{4\mu r_0}{\kappa a_0}$ and $W = \frac{\kappa r_0}{a_0}$, which we may treat as dimensionless parameters. We also remind that $r_0 = \frac{2\pi\xi}{\kappa}$. The main approach is to obtain the solutions to this problem using the `NDEigensystem` function in *Mathematica*, which allows us to solve such an eigenvalue problem corresponding to a given linear differential operator.

3.1.1 On *Mathematica*'s `NDEigensystem`

In solving such eigenvalue problems, the function first converts the eigenvalue equation in (3.1) into a matrix eigenvalue equation. This is done by discretizing $\mathbb{R}^2$ and converting the Hamiltonian operator, $\mathscr{H}$ into a matrix. The wavefunction $\psi(x,y)$ is treated as a vector. Once it has arrived at the matrix equation, it then attempts to find the eigenvectors and eigenvalues to the matrix using the Arnoldi algorithm. The function is implemented such that it computes the solutions to this eigenvalue problem in ascending order of absolute value of the eigenvalue. As the details of the Arnoldi algorithm is beyond the scope of the project, it will not be discussed here. See [15] for details.

3.1.2 Details of the computation

In order to speed up the computation time, we included a spatial scaling factor of $z = 2/G$ in the Hamiltonian. Also, as the algorithm produces the first n lowest eigenvalue by its absolute value, we add a constant shift of $\Delta = 30$ to the Hamiltonian to map the negative eigenvalues to positive values. The resulting eigenvalue after computation is shifted back by Δ. With this, the full Hamiltonian used in our code reads

$$H_{\text{code}} = -\frac{1\text{Ha}}{GW} z^{-2} \left[\nabla^2_{(x,y)} + z^2 U(z\sqrt{(1+\beta)x^2 + (1-\beta)y^2}) \right] + \Delta. \tag{3.3}$$

From a more practical viewpoint, the `NDEigensystem` function in *Mathematica* requires two key ingredients to execute. They are the domain of the problem, in our case, some subset of $\mathbb{R}^2$, and the maximum mesh size, which sets an upper bound on the size of the cells of the discretized domain. We specify a square domain for simplicity, and therefore the relevant parameters we require to generate eigenvalues are the `length` of the domain and the max mesh `size`.

In order to calculate the eigenvalues of the Hamiltonian operator in (2.64) accurately, one approach would be to use a sufficiently large domain length and small mesh size. However, this approach is problematic due to several reasons. Firstly, we do not know a priori what domain lengths and mesh sizes are good enough to produce accurate values for different values of μ and β in the Hamiltonian operator. Second, in the case where we would like to generate the eigenvalues up to a certain level of precision i.e. specified by the number of decimal places, such an approach does not inform us of the degree of precision of the computed eigenvalues. Third, even if we were to fix a large domain length and small mesh size for computation, running the program with such specifications could run into various errors. This includes runtime errors such as `CompiledFunctionError`, the failure of the output of the Arnoldi algorithm to converge or anomalous values returned by the calculation. Fourth, it is computationally inefficient to specify a fixed domain `length` and mesh `size` since it is possible that reasonably good values be returned for other values of those parameters which require less computation time.

Henceforth, to reliably compute the eigenvalues to the Hamiltonian to any level of precision while handling the possibility of various errors and minimizing computational time, we have implemented a *Mathematica* script which handles these various demands.

We describe the key ingredients and steps involved in the algorithm:

1. Prior to calculation, we define a wrapper function which wraps `NDEigensystem` and catches runtime errors thrown by *Mathematica*, including errors which calls `Abort` i.e. a termination of the entire computational process. We handle such errors by slightly changing the mesh `size` and performing fresh calculation.

2. The first step of the calculation involves getting an estimate of the eigenvalue by specifying `size = null` and an initial `length = 30`. The length is chosen to ensure that the wavefunctions are sufficiently far from the boundary of the computational domain for accurate and sufficiently fast computation. In doing so, *Mathematica* performs the calculations with unconstrained mesh size and gives a reasonable estimate of the eigenvalue. This result is used as an initial benchmark to identify anomalous results and lead the subsequent steps of the algorithm towards converging eigenvalues.

3. The computation proceeds with a calculation with the initial parameters settings `length = 30` and `size = 1` in 'length-mode'. The calculated value is compared to the previous result.

3.1. If the absolute value of the result differs by a factor greater than 2 or less than 0.5, it classifies the result as an anomaly, tweaks the parameters by a specified amount and performs the computation again.

3.2. If it is not anomalous, the value is stored and updated in an Association which stores the eigenvalue and its frequency of appearance in the computation.

3.3. If the value is equal to the previous value up to the specified precision, the computation switches to the other mode. (i.e. if it is currently in 'length-mode', it switches to 'size-mode' and vice-versa). In 'length-mode' the `length` will be incremented by 3 while the in 'size-mode' the `size` is decreased by 25%. The computation is then repeated with the new parameter values.

3.4. If the value is not equal to the previous, it proceeds in the existing mode, either 'length-mode' or 'size-mode'. As mentioned in the point above, the parameters are tweaked as such before proceeding with a new calculation.

4. The loop specified in the previous point continues, switching between modes until one eigenvalue in the Association has a frequency value of 3. That eigenvalue is returned as the computation result.

In performing this algorithm, the computed eigenvalues are ensured to have converged up to the specified precision as the computation proceeds with larger domain lengths and smaller mesh sizes. The full *Mathematica* code can be found in Appendix A.1.

3.2 Preliminary results and consistency checks

3.2.1 Exciton binding energy in Phosphorene

In order to test the robustness of the NDEigensystem function and our calculations, we first attempted to reproduce the numerical value of the exciton binding energy in phosphorene of 0.76 eV cited in [14]. We briefly mention how some of these parameters are obtained in the paper, since similar methods are also employed in other papers to obtain these parameters.

For the mass related parameters μ and β, the authors first obtained the band structure of phosphorene using first principles calculations based on density functional theory. The effective masses of the electron and hole along the x, y directions

(corresponding to armchair and zizgzag directions) are then obtained by calculating the curvature of the electronic dispersion near the Γ point. This specifically means making the approximation

$$E_n(k) = E_n(k=0) + \frac{\hbar^2}{2m_{\text{eff}}}k^2 + O(k^3) \tag{3.4}$$

near that point, and reading off the coefficient of the quadratic term in the conduction and valence bands to obtain the effective masses of the electron and hole respectively. This is done for both the x and y directions and therefore gives rise to four effective masses (in units of electron mass), which are quoted in the paper as $\mu_x^e = 0.18 \pm 0.04$, $\mu_y^e = 1.23 \pm 0.01$, $\mu_x^h = 0.13 \pm 0.04$. The quantity μ_y^h is mentioned in the paper to be very large compared to the masses here and its exact value is not specified. From these masses, the total effective mass μ and anisotropy parameter β may be computed. The authors cited these quantities as $\mu = 0.07$ and $\beta = 0.89$.

For the polarizability ξ, the authors used an ab-initio method as well, whose details we shall not consider here. The relevant components of the polarizability tensor are cited as $\xi_{xx} = 4.20\,\text{Å}$, $\xi_{yy} = 3.97\,\text{Å}$. In order to use the Keldysh potential which assumes an isotropic polarizability, the authors took the average value of the two diagonal components, $\xi = 4.1\,\text{Å}$. This leads to some negligence of the anisotropy in polarizability but this is a reasonable approximation to make since the anisotropy is not significant.

Lastly, the phosphorene is assumed to be suspended in vacuum for simplicity, corresponding to $\kappa = 1$. In the future event when we are comparing the model's predictions to experimental values with differing dielectric environments (due to different substrates and protective caps) this dielectric constant should be modified accordingly. Our calculation gives binding energy of 0.762 eV which compares very well to the quoted value of 0.76 eV in [14].

To further demonstrate that the calculated binding energy is reliable, a plot of the lowest eigenstate in anisotropic coordinates is shown in Figure 3.1. The plot domain is from -8 to 8 which is sufficiently distant from the boundary of the calculation domain, which spans -30 to 30 per axis, thus suggesting that boundary effects on the eigenvalue are negligible. Note that the axis are in units of the length scale $r_0 z = 3.78\,\text{Å}$ with $r_0 = 2\pi\xi/\kappa = 25.7\,\text{Å}$, the characteristic length scale of the Keldysh potential in phosphorene and the spatial scaling factor of $z = 2/G = 0.147$. Also, as the plot displays the wavefunction in anisotropic coordinates, the actual wavefunction needs to be obtained by a rescaling as prescribed by (2.55). We do not perform the
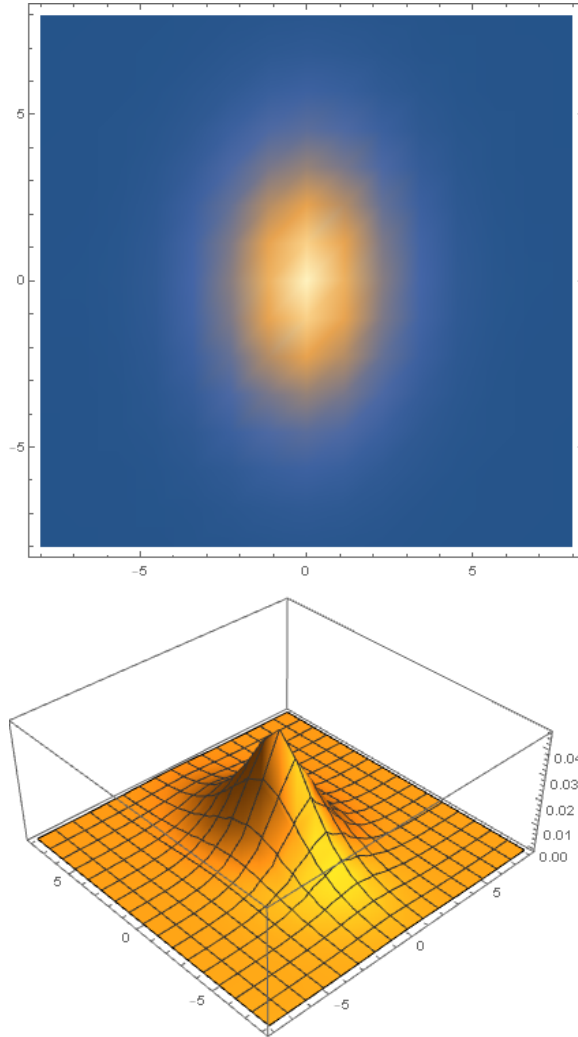
Figure 3.1: Plots of the squared modulus of the exciton spatial wavefunction in anisotropic coordinates. The plot domain is from -8 to 8 units where the axes are in units of the length scale $r_0 z = 3.78\,\text{Å}$.

rescaling here as the main intention is to demonstrate that the wavefunction lies well within the computational domain.

3.2.2   Plot of binding energy versus G
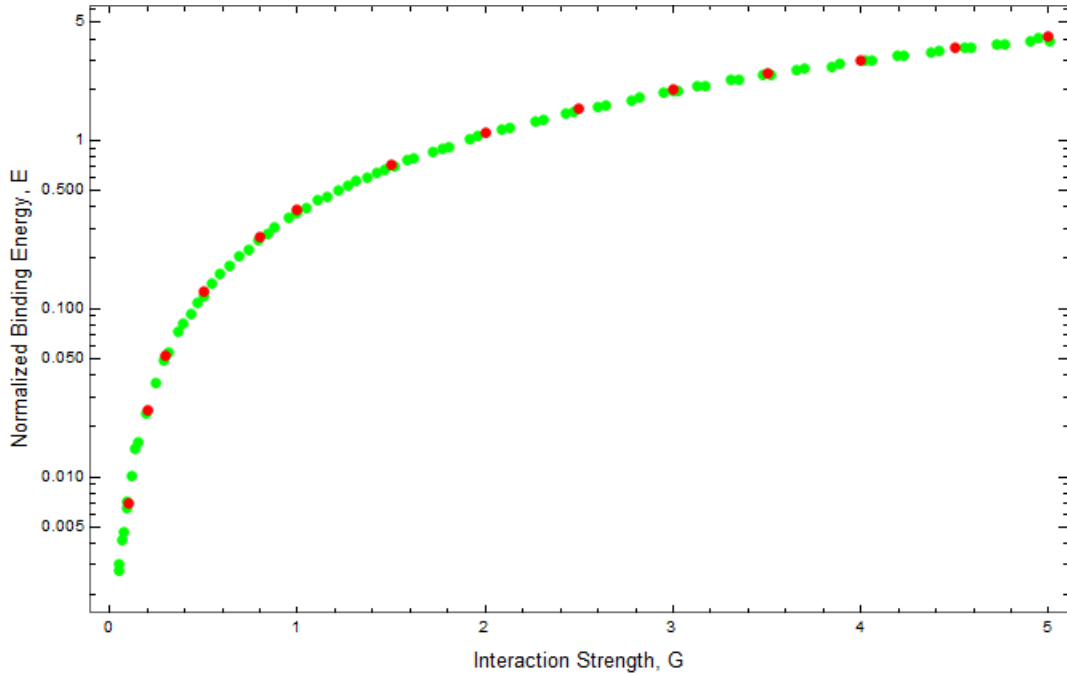
Figure 3.2: Plot of normalized eigenvalues $\mathcal{E}$ versus coupling strength G for $\beta = 0$. In green: Paper's original results [14], extracted using *WebPlotDigitizer*. In red: Our results using *Mathematica*'s NDEigensystem.

As a further consistency check, we attempted to reproduce a plot of the exciton binding energy against the parameter G presented in [14], corresponding to $\beta = 0$. We used *WebPlotDigitizer* [16] to extract the data points of the plot in the paper in a .csv format. We then used the same NDEigensystem code, with slight modification to accommodate G as an input parameter, to reproduce some points of the plot. 14 data points were generated and plotted against these data points for comparison. The result of this calculation is shown in Figure 3.2. The normalized eigenvalue, $\mathcal{E}$, corresponds to the dimensionless Hamiltonian $\mathscr{H}$ in (2.64) and is related to the actual eigenvalue via $E = -\frac{1\text{Ha}}{GW}\mathcal{E}$. As depicted in the figure, we find that there is close agreement between our calculated results and that presented in the paper. This further establishes the reliability of our eigenvalue solving algorithm.

3.3 Exciton binding energy versus mass parameters

In this section, we look at the general trend in the exciton binding energy for various mass parameters μ, β.

We computed the exciton binding energies for phosphorene for various parameter sets within the domains $\mu \in [0.022, 0.702]$ and $\beta = 0$, 0.49, 0.69, 0.89. The relevant plots are shown in Figure 3.3. For each value of β, we observe that the energy varies with μ in a quasi-logarithmic fashion - it starts growing steeply for low values and tapers off as it approaches $\mu = 1$, i.e. when the effective mass gets closer to the electron mass. This is the same behavior displayed in Figure 3.2 when we plotted the normalized energy versus G. Furthermore, for effective masses below 0.1, which is roughly the region applicable to excitons phosphorene, the binding energy displays a relatively rapid variation with the effective mass μ. For instance, varying μ from 0.02 to 0.06 in can give rise to a change in binding energy of up to 0.2 eV. This is a very promising notion since it opens the possibility of varying the binding energy at magnitudes comparable to the order of magnitude of the exciton binding energy in phosphorene.
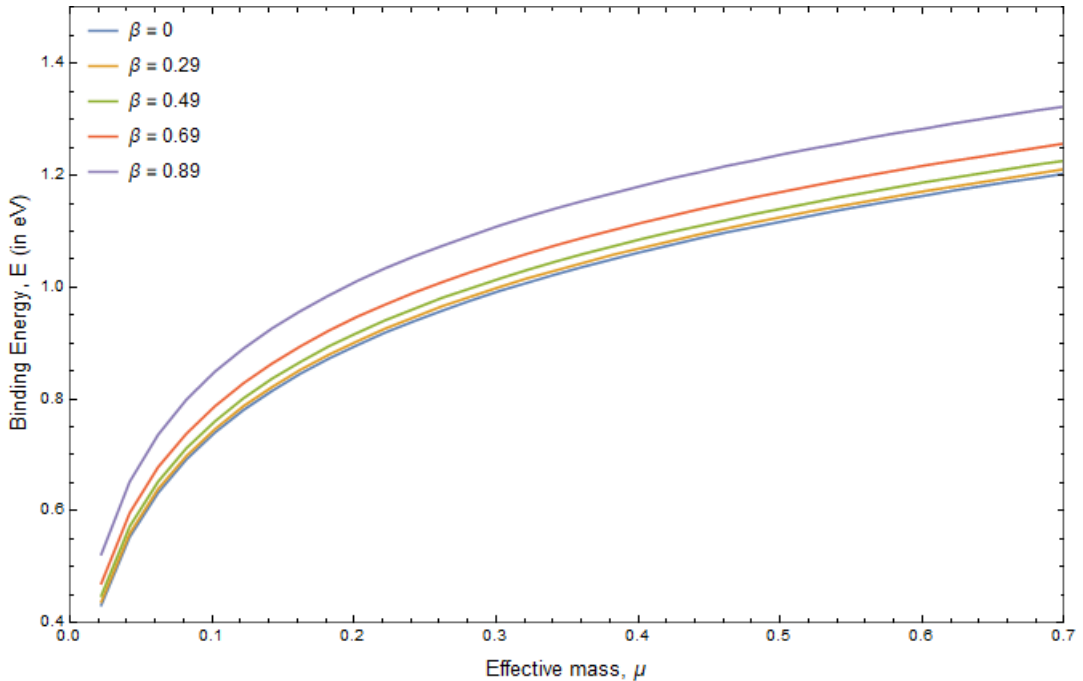

Figure 3.3: Binding energy (in eV) as a function of μ for various β. In the calculations, κ is set to unity.

As for the trend in β, we find that the binding energy varies minimally with the anisotropy relative to the variation induced by a change in effective mass. In addition, for $\beta > 0.8$, we find that within the domain of interest $0.02 < \mu < 0.10$, which is applicable to phosphorene, the binding energy exhibits a greater variation with the effective mass. This means that the situation in phosphorene corresponds to a region in μ, β parameter space in which the exciton binding demonstrates the most sensitivity to variations in the parameters. Therefore, the ability to manipulate the effective masses within the range $0.02 < \mu < 0.10$ and $0.7 < \beta < 0.9$ can give rise to changes in binding energy within the approximate range $0.4 < E < 0.8$ eV.

As a general trend, we also observe that the binding energy is monotonic in both μ and β. The monotonic dependence on μ can be understood by comparing this system with the hydrogen atom, where the dependance of the binding energy on the electron mass is also monotonic. The monotonic dependance of the binding energy on β however is more subtle.

We provide a qualitative argument based on perturbation theory to account for this behavior. Working in anisotropic coordinates, consider the eigenstate, ψ_β for an arbitrary $\beta \in [0,1)$ corresponding to the Hamiltonian and consider a perturbation in β by an infinitesimal positive amount ϵ. We define the quantity $r_\beta = \sqrt{(1+\beta)x^2 + (1-\beta)y^2}$ so we may express the unperturbed potential as $V(r_\beta) = -\frac{e^2}{\kappa r_0}U(r_\beta)$. Expanding about β, the new potential to leading order in ϵ is

$$V(r_{\beta+\epsilon}) = V(r_\beta) + \epsilon\frac{V'(r_\beta)}{2r_\beta}(x^2 - y^2) + O(\epsilon^2). \tag{3.5}$$

The leading correction to the exciton binding energy is proportional to the expectation value of the second term in the state ψ_β i.e.

$$\frac{1}{2}\int \mathrm{d}x\,\mathrm{d}y\,|\psi_\beta(x,y)|^2\frac{V'(r_\beta)}{r_\beta}\left(x^2 - y^2\right) = \left\langle x^2\right\rangle - \left\langle y^2\right\rangle \tag{3.6}$$

where we write the correction in the form of expectation values of the coordinates x and y over the unnormalized distribution given by the quantities in the integrand

$$\frac{1}{2}|\psi_\beta(x,y)|^2\frac{V'(r_\beta)}{r_\beta}. \tag{3.7}$$

We argue that $\left\langle y^2\right\rangle$ is guaranteed to be greater than $\left\langle x^2\right\rangle$ for all $\beta > 0$. Observe first that $|\psi_\beta(x,y)|^2 > 0$ and $\frac{V'(r_\beta)}{r_\beta} > 0$ over $\mathbb{R}^2$. That the derivative of the potential V is positive over this domain can be deduced from the fact that it monotonically increases with distance from the origin. Furthermore, the functions $\frac{V'(r_\beta)}{r_\beta}$ and $|\psi_\beta(x,y)|^2$, when

viewed as a set of contours of constant height, have the characteristic that these contours are elongated along y and compressed along x. As such, the product of the two also shares the same characteristic. This therefore suggests that the expectation value of y is guaranteed to be larger than x and that the leading order correction to the ground state energy is negative i.e. the binding energy will increase under a perturbation on β. To be careful, this argument does not work for $\beta = 0$, where the unnormalized distributions have azimuthal symmetry and the first order correction vanishes. A proper argument must be done for the second order in ϵ for this special case. Nonetheless, the arguments above serve as a sufficient explanation for the monotonic dependance of the binding energy on β.

3.4 Comparison with experimental and ab-initio results

Performing a comparison of the model's predictions against those of experimental measurements or ab-initio calculations from the literature is not clear cut. This is largely due to the fact the electron and hole effective masses for phosphorene vary over a relatively large spread in the literature. Table 3.1 shows the various effective electron and hole masses for each direction, together with the corresponding total effective mass and anisotropy parameter cited in the literature. Note that a value of 1000 implies a value far larger than the other masses.

In order to make reliable comparisons between the model and a reference value from literature, we adopted the following approach. If the effective masses are cited in the paper we are comparing with, we shall use those to obtain μ and β for our calculation of exciton energies. If the masses are not cited in the paper, we shall use the average of the values of the masses of the electron and holes along each direction from the compilation in Table 3.1. The average values that we will use are listed in Table 3.2.

3.4.1 Exciton binding energy

Using the approach laid out in the previous subsection for the effective masses, we calculated the exciton binding energy and compared it to various values reported in the literature. We ensured that the dielectric environment is consistent with what it used in the papers. We briefly give an overview of the techniques used in the papers to arrive at the exciton binding energies.

Table 3.1: Compilation of effective masses of electrons and holes in phosphorene. The entries are sorted by μ.

Reference	μ_x^e	μ_x^h	μ_y^e	μ_y^h	μ	β
Strain-induced gap modification in black phosphorus [5]	0.112	0.117	1.500	1000	0.055	0.926
Electro-mechanical anisotropy of phosphorene (PBE method) [17]	0.128	0.121	1.242	6.475	0.061	0.887
Electric field effect in ultrathin black phosphorus [18]	0.150	0.150	0.700	1.00	0.063	0.691
Excitons in anisotropic two-dimensional semiconducting crystals [14]	0.180	0.130	1.230	1000	0.071	0.884
Landau levels of single-layer and bilayer phosphorene [19]	0.166	0.182	0.846	1.140	0.073	0.696
Electro-mechanical anisotropy of phosphorene (HSE06 method) [17]	0.170	0.155	1.118	6.372	0.080	0.842
Multi-scale approach for strain-engineering of phosphorene [20]	0.200	0.200	1.200	3.900	0.097	0.803
Linear scaling of the exciton binding energy versus the band gap of two-dimensional materials [21]	0.460	0.230	1.120	1.610	0.124	0.623
Phosphorene: an unexplored 2D semiconductor with a high hole mobility [22]	0.300	0.300	2.600	8.300	0.139	0.859

For papers employing ab-initio method, the authors performed first-principles density functional theory and GW-Bethe-Salpeter equation calculations in order to obtain the band structure and optical absorption spectra of phosphorene [12, 23]. The band gap and the optical gap can be extracted respectively from these results, from which the exciton binding energy may be obtained by taking the difference between the two. On the other hand, the experimental papers typically report measuring the photoluminescence or absorption spectra of phosphorene under the impingement of light, with energies above the band gap energy of roughly ~ 2 eV. The optical gap is obtained by reading off the peak photoluminescence intensity [11, 24, 25]. The band gap measurement however may differ in each experimental paper. In [25], the authors obtained a plot of peak photoluminescence intensity against photon excitation energy from which the band gap is determined by identifying the photon energy at

Table 3.2: Average effective masses $\mu_{x/y}^{e/h}$ from literature and the corresponding values for μ and β

μ_x^e	μ_x^h	μ_y^e	μ_y^h	μ	β
0.207	0.176	1.284	1000	0.088	0.843

which the peak intensity increases the fastest. In [24], the band gap was obtained from a separate paper [26], which used scanning tunnelling spectroscopy techniques to identify the band gap in monolayer phosphorene. In [11], they reported that the optical gap and the band gap are indistinguishable based on their peak analysis of the absorption spectrum. Our model's predicted values of the exciton binding energy and the corresponding values obtained in each paper are shown in Table 3.3.

Table 3.3: Comparison between exciton binding energies reported in the literature and obtained from the model

Method	Dielectric Environment	$E_{\text{b,paper}}$ (eV)	$E_{\text{b,model}}$ (eV)
Ab-Initio	Vacuum, $\kappa = 1$ [12, 23]	0.78, 0.80	0.79
Experiment	Sapphire substrate/hBN cap, $\kappa = 3.1$ [11]	0.1	0.35
	SiO$_2$ substrate, $\kappa = 3.9$ [24, 25]	0.30, 0.90	0.28

In calculating these values from the model, we employed the average mass parameters stated in Table 3.2. We find that the predictions of the model agrees well with the values cited from papers employing ab-initio calculations. Comparison with experimental methods gives less numerical agreement but the values are still within the same order of magnitude.

In performing this comparison between the model and the finding in literature, we emphasize here that the aim is to get rough sense of how the values compare and not whether they are in very close agreement. This is due to various reasons: first, due to the large spread of masses in literature, we are basing this comparison on a rough value of μ and β, which may differ from the actual value in phosphorene. Next, the effective model neglects some features of the system (such as the anisotropy of the polarizability) and one therefore cannot expect very high accuracy for the binding energy. Further, some experimentally measured values of the exciton are not in very good agreement with each other, for instance [24] and [25], which have the same dielectric environment but different values of the binding energy possibly due to different experimental techniques used or other unknown factors. Also, if one were to

compare the experimentally measured values based on the dielectric constants κ, and bearing in mind that the binding energy should decrease with more screening, then the fact that the binding energy from [11] is lower than that of [24, 25] is not what is expected and may be at odds with each other.

Nonetheless, we find that the model gives predictions that are reasonable as compared to the values reported from the literature, taking into account the various factors which make this comparison an incomplete one in certain respects. We re-emphasize that the aim of this work is to gauge the sensitivity of excitonic energy levels to stress and not to obtain an exact model that allows for accurate calculations. The key parameters μ and β which enters the model can always be recalibrated in the future once there is a greater consensus on the values of the effective masses in phosphorene in the literature.

3.4.2 Exciton spectrum and eigenstates

In [12], the authors calculated the energy spectrum and wavefunctions of the first four lowest lying energy eigenstates of excitons in phosphorene using ab-initio methods via the GW-Bethe-Salpeter equation. This allows us to perform another check for the robustness of the model. Using the mass parameters in Table 3.2 and our algorithm, we generated the first four lowest eigenvalues and eigenstates of the effective exciton Hamiltonian. A comparison of the exciton energy spectrum obtained from [12] and the squared modulus of the exciton position wavefunctions are shown in Table 3.4 and Figure 3.4 respectively.

Table 3.4: Comparison of exciton energy levels obtained from ab-initio methods and the effective exciton model

Method	Ground Energy (eV)	1st Excited Energy (eV)	2nd Excited Energy (eV)	3rd Excited Energy (eV)
GW Bethe-Salpeter	-0.78	-0.60	-0.50	-0.41
Effective exciton model	-0.79	-0.54	-0.44	-0.36

Comparing the exciton energy spectrum, we observe that the lowest lying exciton energies of both approaches are in relatively good agreement, despite some numerical discrepancy in the higher states. This slight discrepancy possibly arises due to

the negligence of the slight anisotropy in the polarizability tensor of phosphorene. Roughly speaking, the effect of this negligence can be effectively viewed as a slight difference in the anisotropy parameter, β between the model and the situation in the ab-initio method. Viewing the situation in anisotropic coordinates, we see that the ground state is the most localized along the y-axis compared to the higher energy states, which are more delocalized. Thus, it is the least sensitive to differences in β thus giving rise to greater agreement in binding energy.

Comparing the exciton wavefunctions generated via both approaches, we find that the model agrees very well with the ab-initio method from the qualitative point of view. The general shapes of the wavefunction are almost identical. We are unable to perform a more quantitative comparison as this would require the numerical values of the wavefunctions corresponding to the paper, which are not provided. The closest quantitative comparison that can be done is in the scale of the plots. As shown in Figure 3.4, the scale of the elongation of the exciton wavefunction are roughly the same. The ground state of the exciton has a rough length scale of around 2.5 - 3 nm along the x axis and 1 nm along the y axis as suggested by the ab-initio and model results. This conforms to our expectation of a Wannier-Mott exciton, since the distance scales of the exciton which we find here are $\gtrsim 25$ times larger than the typical crystal lattice spacings of the order 1 Å.

In a nutshell, we found that the effective exciton model is able to capture the main features of the excitonic states in phosphorene reasonably well, especially when compared against the ab-initio results. That an effective model is able to produce the excitonic wavefunctions that closely resemble those of ab-initio calculations is remarkable. The excitonic energy spectrum also compare reasonably well with ab-initio predictions, especially the ground binding energy. As such, we are able to proceed with confidence in combining the predictions of the model with the those of the tight-binding model, which will be discussed in the next chapter.
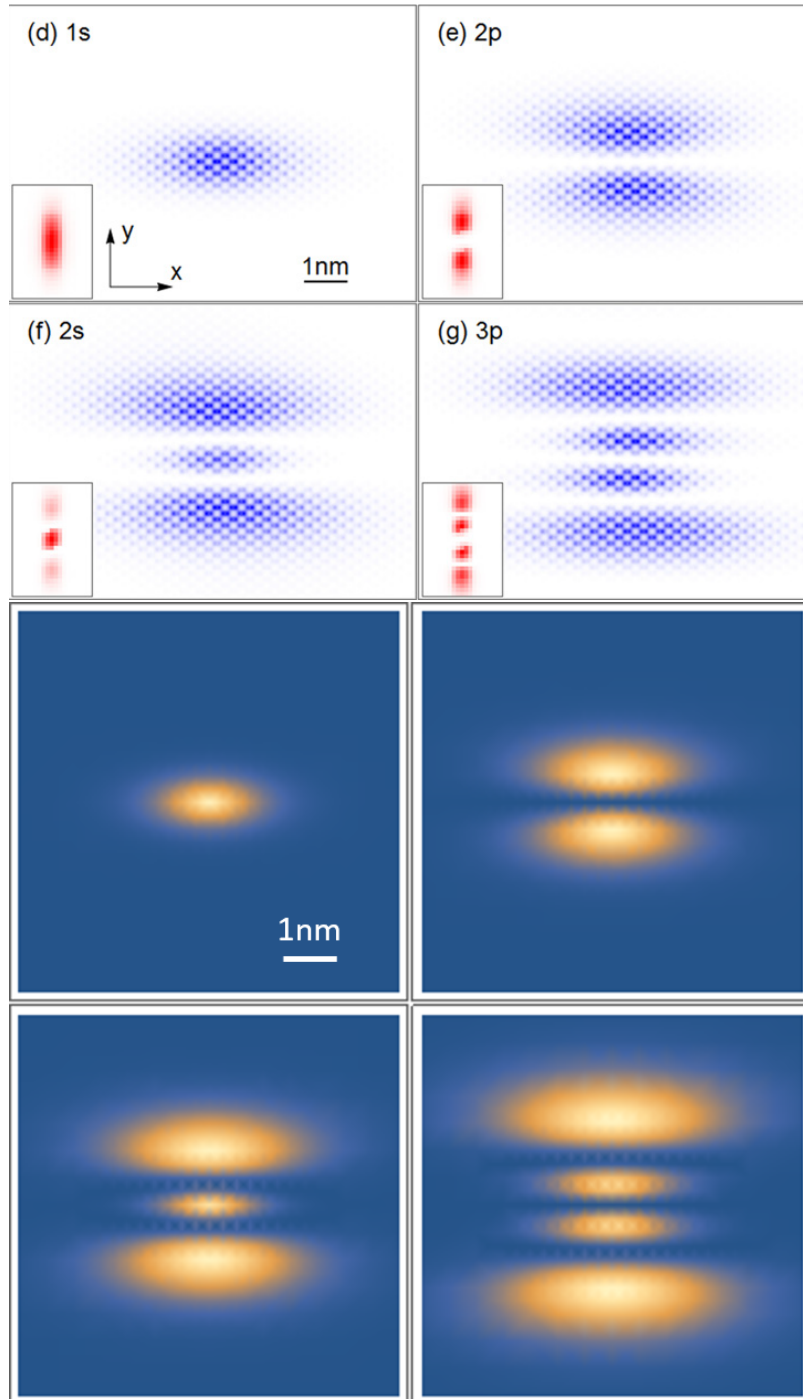
Figure 3.4: Qualitative comparison of first four energy eigenstates (squared modulus of the real space wavefunction) of the exciton from ab-initio GW-Bethe-Salpeter calculations (top) and effective model (bottom).

Chapter 4

Tunability of exciton energy with strain

We have shown that the model used to calculate the exciton energy levels is robust and consistent with the findings in the literature, in spite of the large range of reported values for the effective masses of the electron and hole. In this chapter, we present the methodology adopted to calculate the effect of strain (or stress) on the exciton binding energy. We first explore a tight-binding model which allows us to compute the effective masses in phosphorene from the modified crystal geometry under strain, following closely the methodology proposed by Midtvedt et. al. [20]. We verify the accuracy of this model by comparing the first order dependence of the phosphorene band gap on uniaxial stress with the ab-initio results of Wang et. al. [17]. We then use the predicted effective masses under strain from this model as input parameters of the effective exciton model to obtain a relation between uniaxial stress and the exciton binding energy.

4.1 Effective four-band tight-binding Hamiltonian

We give a brief overview of the tight-binding method which hinges upon the assumption that the atomic orbitals corresponding to each atomic site on the lattice are tightly bound such that one can make the approximation that these orbitals form a complete orthonormal set. As such, let us denote the quantum state corresponding to each orbital per atomic site of a general crystal as

$$|\phi_{\alpha,i}\left(\mathbf{R}\right)\rangle \tag{4.1}$$

where the indices α labels the atoms in a unit cell, i labels the atomic orbitals of that atom and $\mathbf{R}$ denotes the location of the unit cell in the crystal. On a separate front,

we shall assume that the electron-electron interactions may be subsumed with the ionic lattice potential as a total mean-field potential $V(\mathbf{r})$, so that the Hamiltonian of the system reads

$$H = \sum_l H_l \tag{4.2}$$

with

$$H_l = \frac{P_l^2}{2m_e} + V(\mathbf{r}_l). \tag{4.3}$$

where the index l runs over the electrons. The Schrödinger equation for the many-electron system becomes separable under this approximation and we may write the Schrödinger equation in the single-electron picture as

$$H_l \left| \psi_{n\mathbf{k}} \right\rangle = E_{n\mathbf{k}} \left| \psi_{n\mathbf{k}} \right\rangle, \tag{4.4}$$

where we note that $\left| \psi_{n\mathbf{k}} \right\rangle$ are Bloch states due to the translational symmetry of the Hamiltonian. The band structure of the system in this approximation may be obtained by solving for $E_{n\mathbf{k}}$, where n denotes the band index and $\mathbf{k}$ labels the wave-vector. To perform this in the tight-binding method, we first cast the Hamiltonian H_l in the basis of atomic orbitals as in (4.1), where it now reads

$$H = \sum_{\mathbf{R},\mathbf{R}'} \sum_{\alpha,\beta} \sum_{i,j} t_{\alpha i \mathbf{R}; \beta j \mathbf{R}'} \left| \phi_{\alpha,i}\left(\mathbf{R}\right) \right\rangle \left\langle \phi_{\beta,j}\left(\mathbf{R}'\right) \right|, \tag{4.5}$$

where we do away with the index l of the Hamiltonian for cogency. The matrix elements $t_{\alpha i \mathbf{R}; \beta j \mathbf{R}'}$ are known as hoppings as is commonly called in the literature. These quantities are related to the transition amplitude of an electron being initially localized at one atom to being localized at another atom at a slightly later time. In [20], the authors performed this approximation using a basis corresponding to the four atoms in the unit cell of phosphorene and with only one p_z orbital per atom (the atoms in the unit cell are labelled 1 to 4 in Figure 4.1). Therefore, we may drop the index i and let α run from 1 to 4 for our purposes. Together with some relabelling via $\mathbf{R}' = \mathbf{R} + \mathbf{n}$, the Hamiltonian may be slightly simplified to

$$H = \sum_{\mathbf{R},\mathbf{n}} \sum_{\alpha,\beta} t_{\alpha\beta}(\mathbf{n}) \left| \phi_\alpha\left(\mathbf{R}\right) \right\rangle \left\langle \phi_\beta\left(\mathbf{R} + \mathbf{n}\right) \right|. \tag{4.6}$$

where $\mathbf{n}$ denotes a lattice translation vector and we rewrite the hopping as such since it only depends on the atomic sites within each cell and the lattice translation vector.

The band structure may be obtained by switching to the LCAO (linear combination of atomic orbitals) basis, which is defined by a discrete Fourier transform over the unit cells,

$$|\chi_{\alpha,\mathbf{k}}\rangle = \frac{1}{\sqrt{N}} \sum_{\mathbf{R}} e^{i\mathbf{k}\cdot\mathbf{R}} |\phi_\alpha(\mathbf{R})\rangle, \tag{4.7}$$

where N is the number of unit cells in the crystal. One may check that this is a Bloch state and is orthogonal in both indices $\mathbf{k}$ and α. Inserting this into (4.6), we obtain a Hamiltonian which is diagonal in the wave-vector $\mathbf{k}$ i.e.

$$H = \sum_{\mathbf{k}} \sum_{\alpha,\beta,\mathbf{n}} t_{\alpha\beta}(\mathbf{n}) e^{i\mathbf{k}\cdot\mathbf{n}} |\chi_{\alpha,\mathbf{k}}\rangle \langle \chi_{\beta,\mathbf{k}}| \tag{4.8}$$

$$= \sum_{\mathbf{k}} \sum_{\alpha,\beta} \bar{t}_{\alpha\beta}(\mathbf{k}) |\chi_{\alpha,\mathbf{k}}\rangle \langle \chi_{\beta,\mathbf{k}}|. \tag{4.9}$$

Therefore, for each wave-vector $\mathbf{k}$, one needs to diagonalize the 4×4 matrix $\bar{t}_{\alpha\beta}(\mathbf{k})$ labelled by the indices α, β in order to obtain the four-band energies corresponding to these atomic site indices. In [20], the authors introduced eight hopping parameters, t_i, $i = 1, 2, ..8$ (albeit with $t_5 = t_7 = 0$) in order to accurately describe the electronic band structure under stress conditions near the Γ point. These hoppings are obtained by fitting the predictions of the tight-binding model to an ab-initio calculated band structure. In relation to our discussion above, the indices i correspond to a specific set of $(\alpha, \beta, \mathbf{n})$. The specific pairs of atoms with which the hoppings are associated are depicted in Figure 4.1. Referring to the figure, there are several important geometric quantities which are of interest. These are the intra-pucker and inter-pucker angles

$$\theta_1 = 96.5^\circ, \quad \theta_2 = 101.6^\circ, \tag{4.10}$$

the interatomic spacing $d = 2.22\,\text{Å}$, the primitive lattice vectors

$$\mathbf{a}_1 = 2d \left[\cos(\theta_1/2) - \cos(\theta_2)/\cos(\theta_1/2), 0, 0\right]^T \tag{4.11}$$

$$\mathbf{a}_2 = 2d \left[0, \sin(\theta_1/2), 0\right]^T, \tag{4.12}$$

and the interatomic separation vectors within each primitive cell

$$\mathbf{b}_{12} = d \left[\cos(\theta_1/2), -\sin(\theta_1/2), 0\right]^T \tag{4.13}$$

$$\mathbf{b}_{23} = d \left[-\cos(\theta_2)/\cos(\theta_1/2), 0, \sqrt{1 - (\cos(\theta_2)/\cos(\theta_1/2))^2}\right]^T \tag{4.14}$$

$$\mathbf{b}_{24} = d \left[\cos(\theta_2/2), \sin(\theta_1/2), 0\right]^T. \tag{4.15}$$
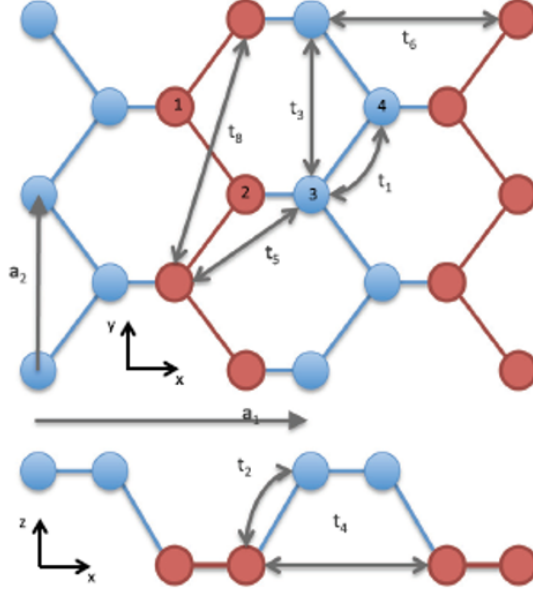
Figure 4.1: Primitive lattice vectors, $\mathbf{a_i}$ and atomic pairs associated with the hoppings, t_i

The key quantities in their model that are of interest to us are the band gap E_g and the effective masses along each direction $m_{x/y}^{e/h}$. The effective masses are obtained by reading off the quadratic coefficients of the dispersion relation $E(k_x, k_y)$ of the valence and conduction band energies. We state the key relations in terms of the hoppings, t_i, and the length of the primitive lattice vectors $\mathbf{a_i}$, $i = 1, 2$ as follows:

$$E_g = 4t_1 + 2t_2 + 4t_3 + 2t_6 + 4t_8 \tag{4.16}$$

$$\mu_x^e = \mu_x^h = \frac{4\hbar^2}{m_e a_1^2} \left[\Delta E + 16(t_2 - 6t_4) - (\Delta E)^{-1} \left(E_g - 8t_2 + 16t_4 \right)^2 \right]^{-1} \tag{4.17}$$

$$\mu_y^e = \frac{2\hbar^2}{m_e a_2^2} (t_1 + 4t_3 + t_4 + 9t_8)^{-1} \tag{4.18}$$

$$\mu_y^h = \frac{2\hbar^2}{m_e a_2^2} (t_1 - 4t_3 + t_4 + 9t_8)^{-1} \tag{4.19}$$

with $\Delta E = 4(t_2 + t_6) - E_g$. The energies and hopping parameters are in eV while the effective masses are dimensionless i.e. in units of electron mass, m_e. The values of the hopping parameters for phosphorene, as cited in [20], are given in Table 4.1.

As one may check, the values of the hoppings correspond to the following values for the band gap and effective masses: $E_g = 1.84$ eV, $\mu_x^e = \mu_x^h = 0.2$, $\mu_y^e = 1.2$, $\mu_y^h = 3.9$.

Table 4.1: List of hopping parameters from [20].

t_1 (eV)	t_2 (eV)	t_3 (eV)	t_4 (eV)	t_6 (eV)	t_8 (eV)
-1.25	4.38	-0.106	-0.34	-0.47	0.09

4.2 Effective masses under stress

In our approach, the effect of stress is to modify the effective masses which enter the effective exciton model via the parameters μ and β. As such, a reliable framework which relates the stresses acting on phosphorene to the effective masses is required before we can compute the response of the exciton binding energy to stress. In this section, we present several key ideas based on [20] which leads a procedure enabling us to compute the effective masses under stress conditions.

4.2.1 Relating stress to hopping parameters

In the tight-binding model, the masses are determined by the hopping parameters. In order to relate stress to the masses, we first need a relation between the applied stress and the hoppings. To do so, we follow the generic treatment in the literature by making the ansatz that the hoppings decay exponentially with the interatomic distances associated with it i.e.

$$t'_i = t_i e^{-\lambda(|\mathbf{R}'_i|/|\mathbf{R}_i|-1)}. \tag{4.20}$$

Here, $\mathbf{R}_i$ is the interatomic separation vector associated with the hopping t_i and the primed and unprimed quantities correspond to stress and equilibrium conditions respectively. The decay constant λ can be determined by fitting to ab-initio calculations. In the notation we introduced above, the hoppings comprise of matrix elements of the form

$$t_{\alpha\beta}(\mathbf{n}) = \langle \phi_\alpha(\mathbf{R})| \left(\frac{P^2}{2m_e} + V(\mathbf{r}) \right) |\phi_\beta(\mathbf{R} + \mathbf{n})\rangle \tag{4.21}$$

which are essentially the overlap integrals between orbitals localized at different atomic sites. The atomic orbitals display an exponentially decaying asymptotic behavior far from the site of localization. Therefore, as the overlap integrals which give rise to hoppings typically involve the overlap between two exponential tails of atomic orbitals localized on different atoms in the tight-binding approximation, we expect the hoppings to also decay exponentially with the interatomic distances.

The effect of uniaxial stress, denoted σ, is captured in $\mathbf{R}'$. The key step is obtaining a relation between stress and the new positions of the atoms in the lattice. This involves knowing the deformation or strain ϵ, which tells us the new locations of the atoms with respect to their original positions under stress.

4.2.2   Stress-strain relation in phosphorene

For a system subject to deformation, we may describe the relation between stress, σ_{ij} and strain, ϵ_{ij} in the elastic regime via Hooke's law $\sigma_{ij} = C_{ijkl}\epsilon_{kl}$ where the repeated indices imply a summation and C_{ijkl} is the stiffness tensor. We use the Voigt notation and describe the stress and strain as six component vectors since they are symmetric 3×3 matrices with only 6 independent components. One may also show that the number of independent components of the stiffness tensor reduces to 9 by symmetry. As such we may write Hooke's law in matrix form

$$
\begin{bmatrix} \sigma_{xx} \\ \sigma_{yy} \\ \sigma_{zz} \\ \sigma_{yz} \\ \sigma_{xz} \\ \sigma_{xy} \end{bmatrix} = \begin{bmatrix} C_{11} & C_{12} & C_{13} & 0 & 0 & 0 \\ C_{21} & C_{22} & C_{23} & 0 & 0 & 0 \\ C_{31} & C_{32} & C_{33} & 0 & 0 & 0 \\ 0 & 0 & 0 & C_{44} & 0 & 0 \\ 0 & 0 & 0 & 0 & C_{55} & 0 \\ 0 & 0 & 0 & 0 & 0 & C_{66} \end{bmatrix} \begin{bmatrix} \epsilon_{xx} \\ \epsilon_{yy} \\ \epsilon_{zz} \\ 2\epsilon_{yz} \\ 2\epsilon_{xz} \\ 2\epsilon_{xy} \end{bmatrix}. \tag{4.22}
$$

In our study, we shall only concern ourselves with in-plane strains ($\epsilon_{zz} = \epsilon_{yz} = \epsilon_{xz} = 0$) due to the limited knowledge of phosphorene's stiffness tensor that is presently available. Specifically, only the quantities $C_{11}, C_{12}, C_{21}, C_{22}, C_{66}$ have been calculated ab-initio in the literature while the other components are unknown, which necessitate the need to make this restriction. We therefore reduce the system of equations above to

$$
\begin{bmatrix} \sigma_{xx} \\ \sigma_{yy} \\ \sigma_{xy} \end{bmatrix} = \begin{bmatrix} C_{11} & C_{12} & 0 \\ C_{12} & C_{22} & 0 \\ 0 & 0 & C_{66} \end{bmatrix} \begin{bmatrix} \epsilon_{xx} \\ \epsilon_{yy} \\ 2\epsilon_{xy} \end{bmatrix}, \tag{4.23}
$$

together with the following condition for the $z-$stresses:

$$
\sigma_{zz} = C_{31}\epsilon_{xx} + C_{32}\epsilon_{yy}. \tag{4.24}
$$

Note that in phosphorene, $C_{12} = C_{21}$ [6]. If we were to invert the relation between stress and strain in this quasi-two-dimensional context, we find that the in-plane stresses $\sigma_{xx}, \sigma_{yy}, \sigma_{xy}$ completely determines the in-plane strains $\epsilon_{xx}, \epsilon_{yy}, \epsilon_{xy}$. These

strains in turn determine a constraint for σ_{zz} as shown in (4.24), which tells us the required $z-$stress to maintain the $z-$strain at zero. In reality, applying stresses purely in the planar directions will result in some compression along z due to the Poisson effect. However, as there is currently a lack of information of the other components of the stiffness tensor, we are unable to account for this in our calculations. Therefore, for the sake of accuracy, we fix $\epsilon_{zz} = 0$ and focus only on planar stresses and strains. Nonetheless, we note that this quasi-two-dimensional situation of planar stresses and strains in practice requires a z-stress prescribed by (4.24) in conjunction with the in-plane stresses in order to be realized physically. The stiffness constants for phosphorene, calculated using ab-initio methods by [20] are shown in Table 4.2.

Table 4.2: Stiffness constants for phosphorene obtained from ab-initio calculations in [20].

C_{11} (GPa nm)	C_{22} (GPa nm)	C_{12} (GPa nm)	C_{66} (GPa nm)
26.2	105.2	18.4	22.4

Note that C_{11} is four times smaller than C_{22} because, as one might expect, it is easier to stretch phosphorene along the puckered armchair direction compared to the zig-zag direction because the former mainly involves flattening the pucker while the latter involves lengthening the interatomic bonds.

4.2.3 Deformation of phosphorene under strain

Using the stress-strain relation (4.23), we may obtain the strain tensor under any planar stresses. The next step would be to determine the new positions of the atoms from the strain tensor, ϵ. For a perfectly continuous elastic material, we may express the relation between the initial positions of the points of the material and the final positions as

$$\mathbf{r}' = (I + \epsilon)\mathbf{r} \tag{4.25}$$

where I is the 3×3 identity matrix. This equation holds true for a typical crystal up till distance scales greater or equal to that of the unit cell. In other words, the primitive lattice vectors $\mathbf{a}_i$ of phosphorene under stress can be written as

$$\mathbf{a}'_i = (I + \epsilon)\mathbf{a}_i \tag{4.26}$$

with

$$\epsilon = \begin{bmatrix} \epsilon_{xx} & \epsilon_{xy} & 0 \\ \epsilon_{xy} & \epsilon_{yy} & 0 \\ 0 & 0 & 0 \end{bmatrix} \tag{4.27}$$

for planar strains. This can be argued on grounds of symmetry. Since the crystal exhibits translational symmetry with respect to the primitive lattice vectors i.e. the crystal can be generated by tessellating the primitive unit cell, if (4.25) holds true for any arbitrarily sized region of the crystal larger than the unit cell, then it should also hold true at the level of the unit cell.

However, at length-scales smaller than the unit cell, which involve the positions of the basis atoms within each unit cell, (4.25) may no longer hold true. As such, one turns to ab-initio methods which minimizes the energy of the crystal under the constraints set by (4.26) in order to determine the new positions of the basis atoms within each unit cell under strain. In [20], the authors performed this kind of ab-initio calculation and came up with an analytic expression which tells us the new positions of the basis atoms under strain. The expressions involve parameters κ_i with $i = 1, 2, ..5$ which correspond to the result of the ab-initio method. According to them, the separation vectors between the basis atoms under strain may be described by

$$\mathbf{b}'_{12} = (I + \epsilon)\,\mathbf{b}_{12} - \mathbf{v}_{||} \tag{4.28}$$

$$\mathbf{b}'_{23} = (I + \epsilon)\,\mathbf{b}_{23} + \mathbf{v} \tag{4.29}$$

$$\mathbf{b}'_{34} = (I + \epsilon)\,\mathbf{b}_{34} - \mathbf{v}_{||} \tag{4.30}$$

with

$$\mathbf{v} = d \begin{bmatrix} \kappa_1 \epsilon_{xx} + \kappa_2 \epsilon_{yy} \\ \kappa_3 \epsilon_{xy} \\ \kappa_4 \epsilon_{xx} + \kappa_5 \epsilon_{yy} \end{bmatrix}. \tag{4.31}$$

The notation $\mathbf{v}_{||}$ denotes the planar component of the vector $\mathbf{v}$. The parameters κ_i are given in Table 4.3.

Table 4.3: The parameters κ_i related to the positions of basis atoms in the unit cell under strain [20]

κ_1	κ_2	κ_3	κ_4	κ_5
0.71	0.27	1.26	-0.39	-0.16

4.2.4 Full calculation procedure

In this subsection, we present a procedure which allows for the calculation of the effective masses under arbitrary uniaxial planar stresses in the elastic regime.

One first specifies the planar stress via the magnitude σ and the angle θ of the uniaxial stress with respect to the x axis i.e. the armchair direction. This suggests the following form for the stress tensor,

$$\sigma_{ij} = \sigma \begin{bmatrix} \cos^2 \theta & \sin \theta \cos \theta \\ \sin \theta \cos \theta & \sin^2 \theta \end{bmatrix}. \tag{4.32}$$

From the stress tensor, one calculates the strain tensor components ϵ_{ij} by inverting the planar stress-strain relation in (4.23)

$$\begin{bmatrix} \epsilon_{xx} \\ \epsilon_{yy} \\ 2\epsilon_{xy} \end{bmatrix} = \begin{bmatrix} S_{11} & S_{12} & 0 \\ S_{21} & S_{22} & 0 \\ 0 & 0 & S_{66} \end{bmatrix} \begin{bmatrix} \sigma \cos^2 \theta \\ \sigma \sin^2 \theta \\ \sigma \sin \theta \cos \theta \end{bmatrix}, \tag{4.33}$$

where S_{ij} is are the components of the compliance tensor which is inverse to the stiffness tensor C_{ij} i.e. $S_{ij}C_{jk} = \delta_{ik}$.

In a separate step, one calculates the interatomic separation $\mathbf{R}_i$ associated to each hopping t_i. The interatomic separation vectors for each hopping are shown in Figure 4.1. Referring to the figure, these vectors may be expressed in terms of the primitive lattice vectors $\mathbf{a}_i$ and the interatomic separation between the basis atoms $\mathbf{b}_{ij}$. The exact relation between these quantities are listed in Table 4.4. Under strained conditions, these vectors have to be replaced by the corresponding primed versions. This involves applying equations (4.26) and (4.30) together with the strain tensor components ϵ_{ij}.

Finally, one calculates the new interatomic distances associated to each hopping, $|\mathbf{R}'_i|$ and applies the ansatz, (4.20) which expresses the decay of each hopping with interatomic distance. In [20], it was found that the exponential ansatz gives good agreement with ab-initio calculation by setting $\lambda = 2$, which shall also adopt. Using these strained hoppings, one may obtain various quantities such as the band gap and the effective masses under strained conditions using the relations in (4.19).

We have implemented the calculation described above in a *Mathematica* notebook which can be found in Appendix A.2. This calculation is crucial as it allows us to compute the effective masses under stressed conditions, which is required for calculation of the exciton binding energy under different stressed conditions.

Table 4.4: Listing of interatomic separation vectors $\mathbf{R}_i$ corresponding to each hopping t_i expression in terms of the primitive lattice vectors $\mathbf{a}_i$ and the separation vectors between basis atoms $\mathbf{b}_{ij}$.

Hopping, t_i	Interatomic separation vector, $\mathbf{R}_i$
t_1	$\mathbf{R}_1 = \mathbf{b}_{34}$
t_2	$\mathbf{R}_2 = \mathbf{b}_{23}$
t_3	$\mathbf{R}_3 = \mathbf{a}_2$
t_4	$\mathbf{R}_4 = \mathbf{a}_1 - \mathbf{b}_{12}$
t_6	$\mathbf{R}_6 = \mathbf{b}_{12} + \mathbf{b}_{23} + \mathbf{b}_{34}$
t_8	$\mathbf{R}_8 = 2\mathbf{a}_2 + \mathbf{b}_{12}$

4.2.5 Band gap versus stress

To ascertain the robustness of the authors' approach in determining the new hoppings for stressed conditions, we compared the relation between the band gap and stress obtained via this approach, to linear order, against the same relation from a separate paper which employs more direct ab-initio calculations [17]. This paper uses two different ab-initio schemes, dubbed PBE (Perdew-Burke-Ernzerhof) and HSE06 (Heyd-Scuseria-Ernzerhof) to arrive at the relations. The two schemes are density functional theory calculations which employ different exchange correlation functionals. The relation between the band gap and uniaxial stress takes the general form

$$E_g(\sigma, \theta) = E_g^0 + \sigma \left(h_{11} \cos^2 \theta + h_{12} \sin \theta \cos \theta + h_{22} \sin^2 \theta \right) \tag{4.34}$$

where E_g^0 is the band gap without stress and the coefficients h_{11}, h_{12}, h_{22}, are dependant on the approach of calculation.

On our part, we used the analytic expressions mapping stresses to band gap in our *Mathematica* notebook and took a linear order expansion of the binding energy E_g as a function of stress σ. We then compared the coefficients of these linear expansion to the one obtained from direct ab-initio methods. These values are listed in Table 4.5. We find that the coefficients are in generally good agreement, with greater numerical agreement for the coefficients h_{11} and h_{22} corresponding to uniaxial stress along the armchair and zigzag directions respectively.

Table 4.5: Comparison of coefficients in the linear expansion of the band gap, E_g as a function of uniaxial stress σ and direction θ

Method	h_{11} (eV GPa^{-1} nm^{-1})	h_{12} (eV GPa^{-1} nm^{-1})	h_{22} (eV GPa^{-1} nm^{-1})
Ab-Initio, PBE	0.138	0.0125	0.025
Ab-Initio, HSE06	0.139	0.022	0.034
Tight-binding	0.154	0.09	0.022

4.3   Exciton binding energy versus uniaxial stresses

Using the procedure laid out in the previous section, we first computed the parameters μ and β for various values of uniaxial stress along the armchair and zigzag directions. To ensure that our results are within the elastic regime, the stresses lie within a domain which give rise to strains up to a maximum of about 8%, taking reference from [20]. Specifically, this corresponds to an upper bound of about 1.9 GPa nm for stresses in the armchair direction and 7.5 GPa nm for the zig-zag direction. We plotted the new effective mass parameters μ and β versus for these uniaxial stress conditions against the strains in the corresponding directions in Figures 4.2 and 4.3.
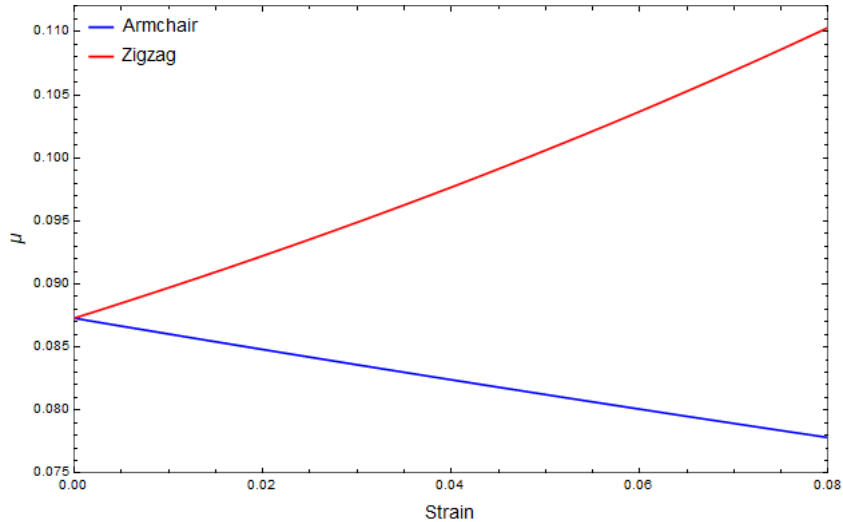

Figure 4.2: Predicted response of the total effective mass of the exciton μ to uniaxial stresses along the armchair and zigzag directions.
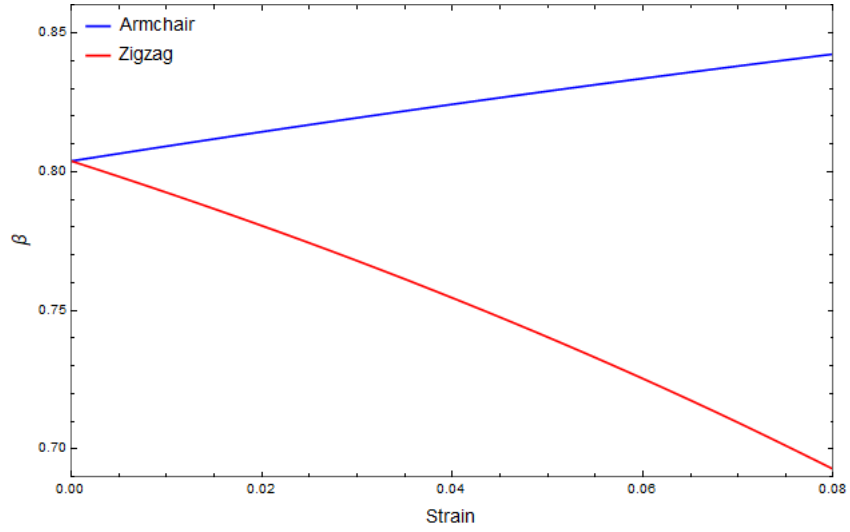
Figure 4.3: Predicted response of the anisotropy parameter β to uniaxial stresses along the armchair and zigzag directions.

We find that the application of uniaxial stress may result in a rather significant change in the parameters involved. In particular, a strain of 8% in the zigzag direction could lead to a significant 20% increase in μ. The same strain leads to a decrease in β by about 12%. However, we find that μ and β respond to uniaxial stress in opposite directions. As the exciton binding energy varies monotonically with both parameters as found in the previous section, this means that the changes brought about by both parameters to the binding energy cancel each other to some degree, therefore reducing the sensitivity of the exciton binding energy to stress.

Figure 4.4: Exciton binding energy versus μ and β

Using the parameter values of μ and β falling within the range suggested by the plots, $\mu \in [0.078, 0.112]$, $\beta \in [0.69, 0.85]$, we generated an `InterpolatingFunction` in *Mathematica* which maps $(\mu, \bet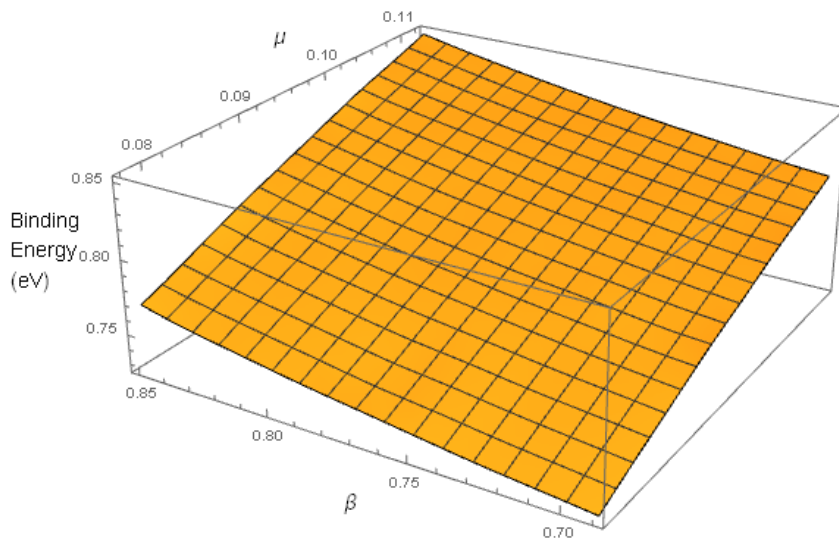a)$ within this domain to the corresponding exciton binding energy, E_B using the algorithm from Chapter 3. A plot of the function $E_B(\mu, \beta)$ is shown in Figure 4.4. We find that within the (μ, β) domain that we are interested in, the binding energy appears to vary almost linearly with respect to μ and β, where the monotonic nature of this variation as mentioned in the earlier chapter is manifest in the plot.

Finally, using this `InterpolatingFunction` and the points of the plots in Figures 4.2 and 4.3, we obtain a relation between the exciton binding energy versus uniaxial stress along the orthogonal directions. The results are shown in Figure 4.5.
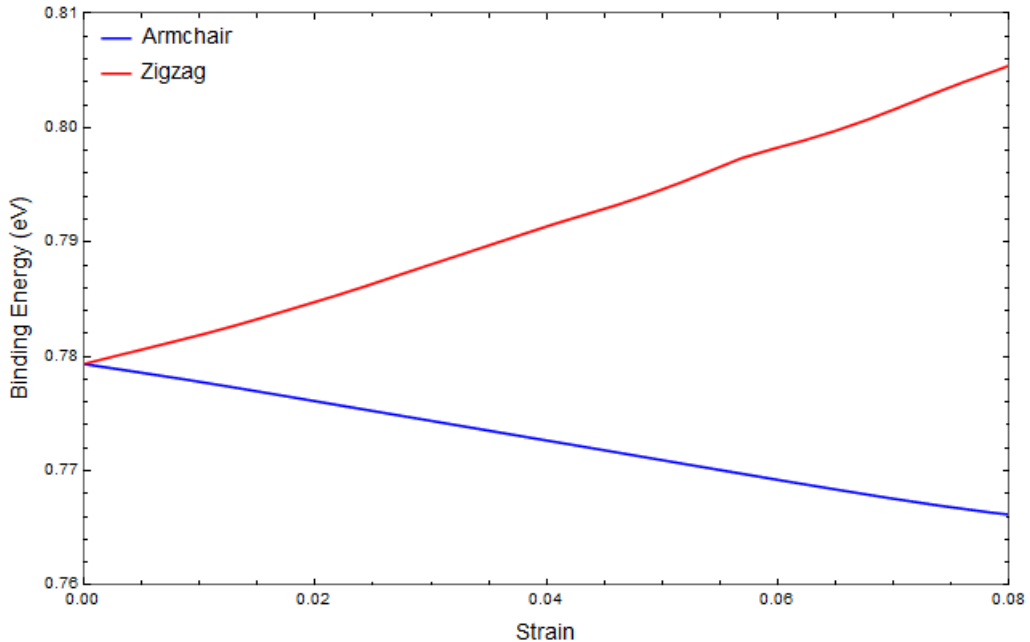
Figure 4.5: Exciton binding energy versus strain

We find that the application of strain in orthogonal directions give rise to changes in the exciton energy in opposite directions as well, similar to the behavior found for the parameters μ and β. The exciton energy can vary by about 0.04 eV under application of stress, which is roughly 5% the magnitude of the exciton binding energy (~ 0.78 eV). In comparison, the band gap of phosphorene (~ 1.8 eV), can vary up to 0.2 eV i.e. about an 11% change of band gap size. To illustrate the significance of the variation of exciton binding energy on the optical gap in stressed conditions, we obtained plots for the optical gap under stresses in both directions with one pair of plots corresponding to the case where we disregard the variation of exciton binding

energy with stress (dashed plots) and another pair which includes this effect (bold plots). These plots are shown in Figure 4.6.
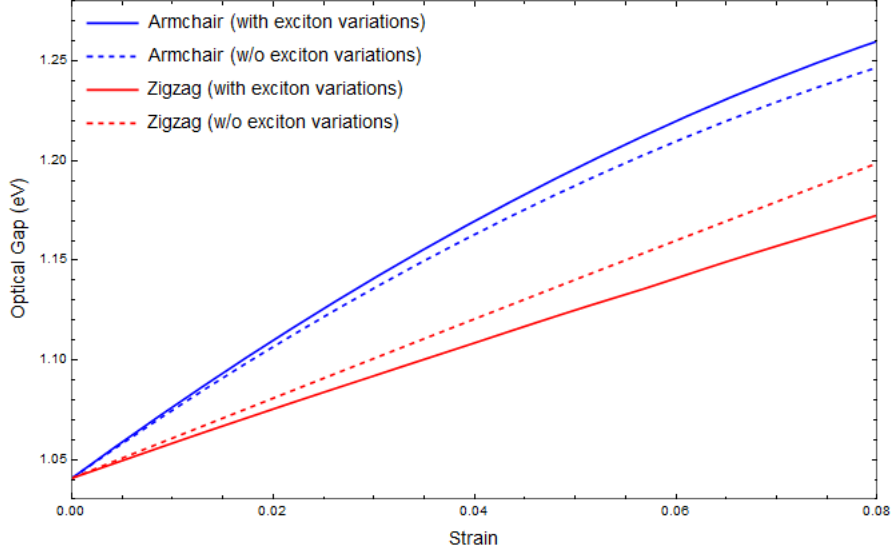
Figure 4.6: Plots of optical gap versus strain: a) Neglecting variations in exciton binding energy (dashed lines), b) Including variations in exciton binding energy (bold lines)

By comparing the dashed and bold plots, we find that the variations of the exciton binding energy with strain are non-negligible even though they are smaller than the variations of the band gap. As the optical gap E_o is given by

$$E_\text{o} = E_\text{bg} - E_\text{x}, \tag{4.35}$$

where E_bg and E_x refer to the band gap and the exciton binding energy respectively, the results suggest that under strains of about 8%, the variations in exciton binding energy ($\Delta E_\text{x} \sim 0.03$ eV) contributes to variations in the optical gap ($E_\text{o} \sim 1.04$ eV in equilibrium) of $\Delta E_\text{x}/E_\text{o} \sim 3\%$. In comparison, the band gap variations under these conditions ($\Delta E_\text{bg} \sim 0.12$ eV) provides the dominant contribution to the variations in the optical gap of $\Delta E_\text{bg}/E_\text{o} \sim 12\%$. Overall, this means that the excitonic contribution to the total optical gap variation is $\sim 20\%$ which is rather significant.

Therefore, we find that while the contribution of variations in exciton binding energy with is smaller than that of the band gap, the models suggest that these effects cannot be ignored in the consideration of the strain tunability of the optical gap of phosphorene.

Chapter 5

Conclusion and Future work

Through the use of an effective exciton model in 2D crystals, a tight-binding model and elasticity theory, we estimate that the exciton binding energy can be varied by about 5% of its original value under strains of up to 8%. We also found that the variation of exciton binding energy under strain contributes non-negligibly to the variations of the optical gap. In particular, the exciton binding energy contributes to roughly 20% of the total variation of the optical gap under the strained conditions we considered. Our findings show that the specific contribution from excitonic effects is essential for an accurate quantitative description of the strain tunability of the optical gap in phosphorene.

Overall, we found that the optical gap can be tuned in excess of 200 meV in this range, or by about 25 meV per 1% of uniaxial deformation. This extremely and unusually high sensitivity can be exploited in optoelectronic sensors. In addition, although there are recent ab-initio reports in the literature addressing the effect of strain in the band structure of this atomically-thin system at the single-particle level, to the best of our knowledge, this work constitutes the first quantitative assessment of the strain-induced modifications of the excitonic spectrum and optical gap in phosphorene.

Through the use of the tight-binding models, we also identified that the key factors which determine the excitonic binding energies, the effective mass μ and anisotropy parameter β, change in the opposite direction in response to strain despite being able to attain relatively significant changes of around 12 - 20 %. As the exciton model yields a binding energy that varies monotonically with both parameters, this suggests that the variations caused by one parameter counter-act the other, thus decreasing the sensitivity of the excitonic binding energy to strain.

The utility of effective models is also manifest in our work. The exciton model is able to reproduce the wavefunctions of the GW-Bethe-Salpeter equations very well

from a qualitative viewpoint. The exciton energy spectrum also compares reasonably well despite some numerical discrepancy in the higher energy states. Also, the tight-binding model is able to reproduce an ab-initio calculated linear order variation of band gap with strain with good agreement. As such, the findings of our work give a reasonable estimate or gauge of the actual sensitivity of the exciton binding energy to strain and its significance in optical gap strain tunability.

Our work also shows that the models provide a good starting point for future efforts to construct more realistic models of excitons in phosphorene, by extending the current approximations. The exciton model can be improved by including two additional effects: the first being the slight anisotropy of the polarizability of phosphorene and the second being the variation of the polarizability with strain. To handle the former, one may use perturbative methods - starting from the Fourier transform of the Keldysh potential in (2.48) - to add an anisotropic correction to the potential. This could improve the agreement between the model's predicted exciton spectrum and that of the GW-Bethe-Salpeter equation. To handle the effect of stress on polarizability, it requires an expression relating the polarizability to the effective masses, which is cited in [27]. With this, the effective mass parameters will inevitably appear in the corrected Keldysh potential which could serve as a more realistic description of the anisotropic screening effects in phosphorene. The effect of stress will enter the corrected potential via the effective masses, giving rise to a 'strain-tunable Keldysh potential'.

The tight-binding model can also be improved by including the effects of z-strains and by moving into the non-elastic regime, where the linear behavior we have observed in our work may no longer hold true. In particular, in this regime, the band gap size can become increasingly smaller [5], which leads to more interesting excitonic effects. This requires the use of ab-initio methods coupled with an improved effective tight-binding model that can capture the effects of such regimes. The extensions of these models could hopefully lead to more realistic and accurate predictions, even more so when there is more consensus in the literature with regard to the effective masses in phosphorene in the near future.

Appendix A

Mathematica Code

A.1   Eigenvalue problem solving

```
1  #!/usr/local/bin/MathematicaScript − script
2  ClearAll["Global`*"];
3
4  (*Important Constants*)
5  (*Bohr radius in Angstroms*)
6  Subscript[a, 0] = 0.529177;
7
8  (*Hartree energy in eV*)
9  Ha = 27.2114;
10
11 (*2D material  polarizabilities  in Angstroms*)
12 \[Xi]xx = 4.20; \[Xi]yy = 3.97;
13 \[Xi]  = (\[Xi]xx + \[Xi]yy)/2;
14
15 (* Dielectric  constant*)
16 \[Kappa] = 1;
17
18 (*W parameter*)
19 W = 2 \[Pi]*\[Xi]/Subscript[a, 0];
20
21 (*No. of states to solve*)
22 n = 1;
23
24 (*Store eigenvalue set frequency*)
25 solFreq = <||>;
26
27 (*Helper functions*)
28 (*Truncate away numbers beyond prescribed precision eg. If
29  precision =3,1.2364\[Rule]1.23*)
30 precRound[num_, precision_] := (
31     If[num > 0, neg = False, neg = True];
32     out = Floor[Abs[num]*10^precision]*1.0*10^(−precision);
33     If[neg, out = −out];
34     Return[out]);
35
```

```mathematica
36  (*Returns True if the numbers are equal up to the prescribed
37  precision. If not, return False*)
38  precEqual[num1_, num2_, precision_] := (
39    rounded1 = precRound[num1, precision];
40    rounded2 = precRound[num2, precision];
41    Return[rounded1 == rounded2])
42
43  (*Solve Eigensystem without exception handling*)
44
45  computeEigen[length_, maxSize_, \[Mu]_, \[Beta]_] := (
46      r0 = 2*\[Pi]*\[Xi]/\[Kappa];
47      G = 4*\[Mu]*r0/(\[Kappa]*Subscript[a, 0]);
48      G = 13.6; W = 48.6;
49      conv = Ha/(G*W); shift = 30; scale = 2/G;
50      L = -(Laplacian[u[x, y], {x, y}] +
51          scale^2*G*\[Pi]/
52          2*(StruveH[0,
53              scale*((1 + \[Beta])*x^2 + (1 - \[Beta])*y^2)^(1/2)] -
54            BesselY[0,
55              scale*((1 + \[Beta])*x^2 + (1 - \[Beta])*y^2)^(1/2)])*
56          u[x, y]) + shift*u[x, y];
57    out = NDEigensystem[L,
58      u, {x, -length, length}, {y, -length, length}, n,
59      Method -> {"Eigensystem" -> {"Arnoldi", "MaxIterations" -> 2000},
60         " SpatialDiscretization " -> {"FiniteElement", {"MeshOptions"
61  -> {"MaxCellMeasure" -> maxSize}}}}];
62    out [[1]] = (out [[1]] - shift )*conv*scale^-2;
63    Return[out]
64    );
65
66  (*Solve Eigensystem with exception handling by tweaking maxSize*)
67  computeEigenRecur[length_, maxSize_, \[Mu]_, \[Beta]_,
68    messageLen_] := (
69    Print[" Calculating with the following parameters/status ... " ];
70    Print["Length:" <> ToString[length] <> ",Size:" <>
71      ToString[maxSize] <> ",errorMessageLen:" <>
72      ToString[messageLen]];
73
74    If [Length[$MessageList] > 80,
75     Abort[]
76     ];
77
78    result = CheckAbort[computeEigen[length, maxSize, \[Mu], \[Beta]],
79      Print[
80       "\nBypassed an abort causing error. Tweaking maxSize...\n"];
81      computeEigenRecur[length, maxSize*1.02, \[Mu], \[Beta],
82       Length[$MessageList]]
83      ];
84
85    If [Length[$MessageList] > messageLen,
86     Print["\nBypassed error. Tweaking maxSize...\n"];
87     result =
88      computeEigenRecur[length, maxSize*1.02, \[Mu], \[Beta],
89       Length[$MessageList]]
```

```
90        ];

91

92        Return[result]
93        );

94

95    (∗Solve Eigensystem while recursing lengthwise or sizewise specified
96    by a string, mode \[Rule] "length", "size".∗)(∗Stop if converged to
97    prescribed precision. Handles anomalous cases.Tracks no.or recursions
98    via n∗)
99    computeEigenMode[mode_, length_, maxSize_, \[Mu]_, \[Beta]_,
100       prevEigenvals_, precision_, n_] := (
101       (∗Solve eigensystem∗)
102       Print["Current assoc.:  " <> ToString[solFreq]];
103       result =
104        computeEigenRecur[length, maxSize, \[Mu], \[Beta],
105         Length[$MessageList]];

106

107       eigenVals = result [[1]];
108       Print[" eigenVals: " <> ToString[eigenVals]];
109       Print[" eigenVals vs Prev eigenVals: " <> ToString[eigenVals] <>
110         ", " <> ToString[prevEigenvals] <> "\n"];

111

112       (∗Updates length or maxSize according to mode∗)
113       If [mode == "length",
114        newlength = length + 2; newmaxSize = maxSize,
115        newlength = length; newmaxSize = maxSize∗0.75
116        ];

117

118       (∗ If result is anomalous,
119       skip to next length while preserving prevEigenval and no.of valid
120    recursions ∗)
121       If [Mean[Abs[eigenVals/prevEigenvals]] > 2,
122        Print["Result anomalous.\n"];
123        Return[
124         computeEigenMode[mode, newlength, newmaxSize, \[Mu], \[Beta],
125          prevEigenvals, precision, n]]
126        ];

127

128       (∗ If code has gone past the above, add result to solFreq∗)
129       If [! KeyExistsQ[solFreq, precRound[eigenVals, precision ]],
130         solFreq [precRound[eigenVals, precision ]] = 0;];
131       solFreq [precRound[eigenVals, precision ]]++;

132

133       (∗ If not anomalous, check for convergence with non−
134       adjacent calculations ∗)
135       If [ solFreq [precRound[eigenVals, precision ]] == 3,
136        Print["Converged with past calculations. Returning ..."];
137        Return[{n, length, maxSize, result }]
138        ];

139

140       (∗ If result is not anomalous but not equal up to precision,
141       skip to next length & update preveigenVals and no.of valid
142    recursions ∗)
143        If [! precEqual[eigenVals, prevEigenvals, precision ],
```

59

```
144        Print["Not␣converged.␣␣Proceed␣further.\n"];
145        Return[
146         computeEigenMode[mode, newlength, newmaxSize, \[Mu], \[Beta],
147          eigenVals, precision, n + 1]]
148        ];
149
150      Return[{n, length, maxSize, result}]
151      );
152
153  (*Computes eigensolution, iterating and oscillating over length and
154  size params*)
155  computeEigenFull[initLength_, initMaxSize_, \[Mu]_, \[Beta]_,
156      approxEigenvals_, precision_] := (
157    (* Variables to be updated during loop*)
158    length = initLength; size = initMaxSize;
159    eigenVals = approxEigenvals;
160    calls = 0; mode = "length"; currMaxIter = Null;
161
162    (*Breaks if no.of computeEigenMode calls is 2 or more and the
163  maximum iteration of the last call is 1*)
164    While[calls > 1 && currMaxIter > 1 || calls <= 1,
165     Print["Current␣mode:␣" <> mode];
166     {currMaxIter, length, size, eigenSol} =
167      computeEigenMode[mode, length, size, \[Mu], \[Beta], eigenVals,
168       precision, 1];
169     eigenVals = eigenSol[[1]];
170
171     Print["Completed␣" <> mode <> "wise␣recursion␣with␣..."];
172     Print["No.␣of␣recursions:␣" <> ToString[currMaxIter]];
173     Print[
174      "Current␣length:␣" <> ToString[length] <> ",␣Current␣maxSize:␣" <>
175       ToString[size] <> ",␣Current␣eigenVals:␣" <>
176      ToString[eigenVals] <> "\n"];
177
178     (*Break loop if solFreq reaches 3*)
179     If[solFreq[precRound[eigenVals, precision]] == 3,
180      Print["Returning␣value␣due␣to␣solFreq␣convergence.."];
181      Break[]
182      ];
183
184     (*Update params based on output*)
185     If[mode == "length",
186      mode = "size"; size = size*0.75,
187      mode = "length"; length = length + 2
188      ];
189
190     calls ++;
191     ];
192
193    (*Only return eigenVals, eigenvector*)
194    res = eigenSol;
195
196    (*Round off eigenvals to precision*)
197    res[[1]] = precRound[#, precision] & /@ res[[1]];
```

60

```
198
199     Return[res]
200     );
201
202  (*Get approximate eigenvalues  for  reference*)
203  computeEigenApprox[length_, \[Mu]_, \[Beta]_] := (
204      approxEigenvals = computeEigen[length, Null, \[Mu], \[Beta ]][[1]];
205      Return[approxEigenvals]
206      );
207
208  (*Actual  full  calculation  of  eigenvalues*)
209  runCalc[ length_ ,  precision_ ,  \[Mu]_, \[Beta]_] := (
210      (*Pre-loop:Determine approximate eigenvalue*)
211      Print[" Computing eigenvalues for Keldysh potential with" ];
212      Print[" Initial  domain length: " <> ToString[length]];
213      Print[" Precision : " <> ToString[precision] <> " decimal places"];
214      Print["\[Mu] = " <> ToString[\[Mu]] <> ", \[Beta] = " <>
215        ToString[\[Beta]] <> ", \[Kappa] = " <> ToString[\[Kappa]]];
216      Print["Performing pre-calc. to obtain approx. lowest eigenvalues
217  ..." ];
218      {tPre, approxEigenvals} =
219       AbsoluteTiming[computeEigenApprox[length, \[Mu], \[Beta]]];
220      solFreq [precRound[approxEigenvals,  precision ]] = 1;
221      Print["Approx. lowest eigenvalue : " <> ToString[approxEigenvals]];
222
223      (*Actual calc*)
224      Print["\nBegin actual calc." ];
225      {tCalc,  results } =
226       AbsoluteTiming[
227        computeEigenFull[length, 1, \[Mu], \[Beta], approxEigenvals,
228          precision ]];
229      {eigenVals,  sols} = results ;
230      Print[" Error messages: " <> ToString[$MessageList]];
231      Print[" Total calc . time: " <> ToString[tCalc + tPre]];
232      Print[" Eigenvals : " <> ToString[eigenVals] <> "\n"];
233
234      (*Empty solFreq for  further  calculations *)
235      solFreq = <||>;
236      Print["Emptied solFreq: " <> ToString[solFreq]];
237
238      Return[eigenVals];
239      );
240
241  (*Main*)
242  cmdLine = {};
243  If[$OperatingSystem == "Windows",
244    cmdLine = Rest[$CommandLine][[3 ;;]],
245    cmdLine = Rest[$ScriptCommandLine]];
246
247  dir = cmdLine[[1]]; length = ToExpression[cmdLine[[2]]]; precision =
248   ToExpression[cmdLine[[3]]];
249  SetDirectory[dir ];
250  stream = OpenWrite["allConvAC.log", FormatType -> OutputForm];
251  AppendTo[$Output, stream];
```

61

```
252  out = runCalc[length, precision, 0.07, 0.89];
253
254  (*Post−calc*)
255  (*Save results*)
256  Print["Saving results to m file ..."]
257  out >> "allConvAC_out.m";
258  Print["Done."]
259
260  (*Close stream for log.txt*)
261  Close[stream];
```

A.2   Computation of effective mass parameters from stress

```
 1  SetDirectory[NotebookDirectory[]];
 2  (*Multi−scale Approach Hoppings in eV*)
 3  t1 = −1.25; t2 = 4.38; t3 = −0.106;
 4  t4 = −0.34; t6 = −0.47; t8 = 0.09;
 5  (*Energy diff in last 2 bands, E4−E1 and cond and val bands, E3−E2*)
 6  (*\[CapitalDelta]E=6.9*2;Eg=1.83;*)
 7
 8  (* Inter−atomic spacing in Angstroms*)
 9  d = 2.22;
10  (* Intra− and Inter−pucker angles in Radians*)
11  \[Theta]1 = 96.5*2*\[Pi]/360; \[Theta]2 = 101.9*2*\[Pi]/360;
12
13  (*Equilibrium vectors*)
14  (*Primitive lattice vectors − ac and zz i.e. x and y*)
15  a1 = {2*d*(Cos[\[Theta]1/2] − Cos[\[Theta]2]/Cos[\[Theta]1/2]), 0,
16     0}; a2 = {0, 2*d*Sin[\[Theta]1/2], 0};
17  (*Lattice vectors between atoms i,j*)
18  b12 = d*{Cos[\[Theta]1/2], −Sin[\[Theta]1/2], 0}; b23 =
19   d*{−(Cos[\[Theta]2]/Cos[\[Theta]1/2]),
20     0, (1 − (Cos[\[Theta]2]/Cos[\[Theta]1/2])^2)^(1/2)};
21  b34 = d*{Cos[\[Theta]1/2], Sin[\[Theta]1/2], 0};
22
23  (*Strain tensor, identity, plane projector, parity*)
24  u[uxx_, uyy_, uxy_] := {{uxx, uxy, 0}, {uxy, uyy, 0}, {0, 0, 0}};
25  II = IdentityMatrix[3];
26  Pxy = {{1, 0, 0}, {0, 1, 0}, {0, 0, 0}};
27  Prx = {{−1, 0, 0}, {0, 1, 0}, {0, 0, 1}};
28  Pry = {{1, 0, 0}, {0, −1, 0}, {0, 0, 1}};
29
30  (*Correction vector due to departure from Cauchy born approximation −
31  from ab initio *)
32  k1 = 0.71; k2 = 0.27; k3 = 1.26; k4 = −0.39; k5 = −0.16;
33  v[uxx_, uyy_, uxy_] := d*{k1*uxx + k2*uyy, k3*uxy, k4*uxx + k5*uyy};
34
35  (*Strained primitive lattice vectors*)
36  A1[uxx_, uyy_, uxy_] := (II + u[uxx, uyy, uxy]).a1;
37  A2[uxx_, uyy_, uxy_] := (II + u[uxx, uyy, uxy]).a2;
38
39  (*Strained interatomic vectors*)
40  B12[uxx_, uyy_, uxy_] := (II + u[uxx, uyy, uxy]).b12 −
41     Pxy.v[uxx, uyy, uxy];
42  B23[uxx_, uyy_, uxy_] := (II + u[uxx, uyy, uxy]).b23 +
43     v[uxx, uyy, uxy];
44  B34[uxx_, uyy_, uxy_] := (II + u[uxx, uyy, uxy]).b34 −
45     Pxy.v[uxx, uyy, uxy];
46
47  Len[v_] := (v[[1]]^2 + v[[2]]^2 + v[[3]]^2)^(1/2);
48  (* Fractional change in distance per Hopping*)
49  dt1[uxx_, uyy_, uxy_] := (Len[B34[uxx, uyy, uxy]]/Len[b34]) − 1;
```

```
50  dt2[uxx_, uyy_, uxy_] := (Len[B23[uxx, uyy, uxy]]/Len[b23]) − 1;
51  dt3[uxx_, uyy_, uxy_] := (Len[A2[uxx, uyy, uxy]]/Len[a2]) − 1;
52  dt4[uxx_, uyy_,
53     uxy_] := (Len[A1[uxx, uyy, uxy] − B12[uxx, uyy, uxy]]/
54        Len[a1 − b12]) − 1;
55  dt6[uxx_, uyy_,
56     uxy_] := (Len[
57        B12[uxx, uyy, uxy] + B23[uxx, uyy, uxy] + B34[uxx, uyy, uxy]]/
58        Len[b12 + b23 + b34]) − 1;
59  dt8[uxx_, uyy_,
60     uxy_] := (Len[2∗A2[uxx, uyy, uxy] + B12[uxx, uyy, uxy]]/
61        Len[2∗a2 + b12]) − 1;
62
63  (∗Decay constant∗)
64  \[Beta] = 2;
65  (∗Strained hoppings∗)
66  T1[uxx_, uyy_, uxy_] := t1∗Exp[−\[Beta]∗dt1[uxx, uyy, uxy]];
67  T2[uxx_, uyy_, uxy_] := t2∗Exp[−\[Beta]∗dt2[uxx, uyy, uxy]];
68  T3[uxx_, uyy_, uxy_] := t3∗Exp[−\[Beta]∗dt3[uxx, uyy, uxy]];
69  T4[uxx_, uyy_, uxy_] := t4∗Exp[−\[Beta]∗dt4[uxx, uyy, uxy]];
70  T6[uxx_, uyy_, uxy_] := t6∗Exp[−\[Beta]∗dt6[uxx, uyy, uxy]];
71  T8[uxx_, uyy_, uxy_] := t8∗Exp[−\[Beta]∗dt8[uxx, uyy, uxy]];
72
73  (∗Band gap versus Hoppings∗)
74  Eg[t1_, t2_, t4_, t6_, t8_] := 4 t1 + 2 t2 + 4 t4 + 2 t6 + 4 t8;
75  \[CapitalDelta]E[t1_, t2_, t4_, t6_, t8_] :=
76     4∗(t2 + t6) − Eg[t1, t2, t4, t6, t8];
77
78  (∗Band Gap versus Strain∗)
79  EgS[uxx_, uyy_, uxy_] :=
80     Eg[T1[uxx, uyy, uxy], T2[uxx, uyy, uxy], T4[uxx, uyy, uxy],
81      T6[uxx, uyy, uxy], T8[uxx, uyy, uxy]];
82
83
84  (∗Compare eqn 15 in paper against our result∗)
85  Series[EgS[x, y, 0], {x, 0, 1}, {y, 0, 1}];
86  (0.11 t1 + 0.10 t2 − 4.63 t4 − 0.65 t6 + 0.02 t8)∗2∗0.05;
87  EgS[0.05, 0.0, 0.00] − (4 t1 + 2 t2 + 4 t4 + 2 t6 + 4 t8);
88
89  (−1.5 t1 + 0.13 t2 − 1.64 t4 + 0.33 t6 − 3.54 t8)∗2∗0.05;
90  EgS[0.00, 0.05, 0.00] − (4 t1 + 2 t2 + 4 t4 + 2 t6 + 4 t8);
91  (∗Convert Strain to Stress using Stiffness from Electro−mech paper∗)
92  C11 = 26.2; C12 = 18.4; C22 = 105.2; C66 = 22.4;
93  c = {{C11, C12}, {C12, C22}};
94  \[Epsilon]xx[\[Sigma]xx_, \[Sigma]yy_] := (Inverse[
95        c].{\[Sigma]xx, \[Sigma]yy}) [[1]];
96  \[Epsilon]yy[\[Sigma]xx_, \[Sigma]yy_] := (Inverse[
97        c].{\[Sigma]xx, \[Sigma]yy}) [[2]];
98  \[Epsilon]xy[\[Sigma]xy_] := 0.5∗\[Sigma]xy/C66;
99
100 (∗Stressed band gap∗)
101 sEgS[\[Sigma]xx_, \[Sigma]yy_, \[Sigma]xy_] :=
102    EgS[\[Epsilon]xx[\[Sigma]xx, \[Sigma]yy], \[Epsilon]yy[\[Sigma]xx,
103 \[Sigma]yy], \[Epsilon]xy[\[Sigma]xy]];
```

```
104
105  (*Compare band−gap versus strain relation  with  Electro−mech paper*)
106  BG[\[Sigma]_] := sEgS[\[Sigma]*cos^2, \[Sigma]*sin^2, \[Sigma]*cossin];
107
108  (*Compare with result  from  electro−mechanical: *)
109  (*BG[x]=0.89+(0.1375 cos^2+0.0125 cos sin+0.025 sin^2)x*)
110  Series[BG[\[Sigma]], {\[Sigma], 0, 1}]
111
112  (* Effective  masses versus Hoppings*)
113  (*For mhx and mex, value doesn't match paper, changed 16 to 8*)
114  \[HBar]2 = (1.0545*10^−34)^2/(10^−20*9.11*10^−31*1.602*10^−19);
115  mhx[t1_, t2_, t4_, t6_, t8_, a1_] := \[HBar]2/(2*Len[a1]^2)*16/
116      2*(\[CapitalDelta]E[t1, t2, t4, t6, t8] +
117         16*(t2 − 6 t4) − (Eg[t1, t2, t4, t6, t8] − 8 t2 +
118            16 t4)^2*(\[CapitalDelta]E[t1, t2, t4, t6, t8])^−1)^−1;
119  mex[t1_, t2_, t4_, t6_, t8_, a1_] := mhx[t1, t2, t4, t6, t8, a1];
120  mhy[t1_, t3_, t4_, t8_,
121      a2_] := −(\[HBar]2/(2*Len[a2]^2))*4*(t1 − 4 t3 + t4 + 9 t8)^−1;
122  mey[t1_, t3_, t4_, t8_,
123      a2_] := −(\[HBar]2/(2*Len[a2]^2))*4*(t1 + 4 t3 + t4 + 9 t8)^−1;
124
125  (*Strained masses*)
126  Mhx[uxx_, uyy_, uxy_] :=
127    mhx[T1[uxx, uyy, uxy], T2[uxx, uyy, uxy], T4[uxx, uyy, uxy],
128     T6[uxx, uyy, uxy], T8[uxx, uyy, uxy], A1[uxx, uyy, uxy]];
129  Mex[uxx_, uyy_, uxy_] := Mhx[uxx, uyy, uxy];
130  Mhy[uxx_, uyy_, uxy_] :=
131    mhy[T1[uxx, uyy, uxy], T3[uxx, uyy, uxy], T4[uxx, uyy, uxy],
132     T8[uxx, uyy, uxy], A2[uxx, uyy, uxy]];
133  Mey[uxx_, uyy_, uxy_] :=
134    mey[T1[uxx, uyy, uxy], T3[uxx, uyy, uxy], T4[uxx, uyy, uxy],
135     T8[uxx, uyy, uxy], A2[uxx, uyy, uxy]];
136
137  (*Strained  parameters*)
138  \[Mu]x[uxx_, uyy_, uxy_] := 0.5*Mhx[uxx, uyy, uxy];
139  \[Mu]y[uxx_, uyy_, uxy_] :=
140    Mey[uxx, uyy, uxy]*
141    Mhy[uxx, uyy, uxy]/(Mey[uxx, uyy, uxy] + Mhy[uxx, uyy, uxy]);
142  \[Mu][uxx_, uyy_,
143      uxy_] := \[Mu]x[uxx, uyy,
144      uxy]*\[Mu]y[uxx, uyy,
145       uxy]/(\[Mu]x[uxx, uyy, uxy] + \[Mu]y[uxx, uyy, uxy]);
146  \[Beta]\[Beta][uxx_, uyy_,
147      uxy_] := (\[Mu]y[uxx, uyy, uxy] − \[Mu]x[uxx, uyy, uxy])/(\[Mu]x[
148        uxx, uyy, uxy] + \[Mu]y[uxx, uyy, uxy]);
149
150  (*Stressed  masses*)
151  sMhx[\[Sigma]xx_, \[Sigma]yy_, \[Sigma]xy_] :=
152    Mhx[\[Epsilon]xx[\[Sigma]xx, \[Sigma]yy], \[Epsilon]yy[\[Sigma]xx, \
153    \[Sigma]yy], \[Epsilon]xy[\[Sigma]xy]];
154  sMex[\[Sigma]xx_, \[Sigma]yy_, \[Sigma]xy_] :=
155    sMhx[\[Sigma]xx, \[Sigma]yy, \[Sigma]xy];
156  sMhy[\[Sigma]xx_, \[Sigma]yy_, \[Sigma]xy_] :=
157    Mhy[\[Epsilon]xx[\[Sigma]xx, \[Sigma]yy], \[Epsilon]yy[\[Sigma]xx, \
```

```
158  \[Sigma]yy], \[Epsilon]xy[\[Sigma]xy]];
159  sMey[\[Sigma]xx_, \[Sigma]yy_, \[Sigma]xy_] :=
160    Mey[\[Epsilon]xx[\[Sigma]xx, \[Sigma]yy], \[Epsilon]yy[\[Sigma]xx, \
161  \[Sigma]yy], \[Epsilon]xy[\[Sigma]xy]];
162
163  (*Stressed parameters*)
164  s\[Mu]x[\[Sigma]xx_, \[Sigma]yy_, \[Sigma]xy_] := \
165  \[Mu]x[\[Epsilon]xx[\[Sigma]xx, \[Sigma]yy], \[Epsilon]yy[\[Sigma]xx, \
166  \[Sigma]yy], \[Epsilon]xy[\[Sigma]xy]];
167  s\[Mu]y[\[Sigma]xx_, \[Sigma]yy_, \[Sigma]xy_] := \
168  \[Mu]y[\[Epsilon]xx[\[Sigma]xx, \[Sigma]yy], \[Epsilon]yy[\[Sigma]xx, \
169  \[Sigma]yy], \[Epsilon]xy[\[Sigma]xy]];
170  s\[Mu][\[Sigma]xx_, \[Sigma]yy_, \[Sigma]xy_] := \[Mu][\[Epsilon]xx[\
171  \[Sigma]xx, \[Sigma]yy], \[Epsilon]yy[\[Sigma]xx, \[Sigma]yy], \
172  \[Epsilon]xy[\[Sigma]xy]];
173  s\[Beta]\[Beta][\[Sigma]xx_, \[Sigma]yy_, \[Sigma]xy_] := \[Beta]\
174  \[Beta][\[Epsilon]xx[\[Sigma]xx, \[Sigma]yy], \
175  \[Epsilon]yy[\[Sigma]xx, \[Sigma]yy], \[Epsilon]xy[\[Sigma]xy]];
176
177  (*to see stress needed for 8% deformation*)
178  (*x-Stress vs x-Strain*)
179  stressStrainx =
180    Table[{\[Sigma], \[Epsilon]xx[\[Sigma], 0]}, {\[Sigma], 0, 1.9,
181      0.1}];
182
183  (*y-stress vs y-strain*)
184  stressStrainy =
185    Table[{\[Sigma], \[Epsilon]yy[0, \[Sigma]]}, {\[Sigma], 0, 7.5,
186      0.1}];
187
188  (*Stress induced parameters, per direction *)
189  acMu = Table[{\[Epsilon]xx[\[Sigma], 0],
190      s\[Mu][\[Sigma], 0, 0]}, {\[Sigma], 0, 1.9, 0.1}];
191  acBeta = Table[{\[Epsilon]xx[\[Sigma], 0],
192      s\[Beta]\[Beta][\[Sigma], 0, 0]}, {\[Sigma], 0, 1.9, 0.1}];
193  acBE = Table[{\[Epsilon]xx[\[Sigma], 0],
194      sEgS[\[Sigma], 0, 0]}, {\[Sigma], 0, 1.9, 0.1}];
195
196  zzMu = Table[{\[Epsilon]yy[0, \[Sigma]],
197      s\[Mu][0, \[Sigma], 0]}, {\[Sigma], 0, 7.5, 0.25}];
198  zzBeta = Table[{\[Epsilon]yy[0, \[Sigma]],
199      s\[Beta]\[Beta][0, \[Sigma], 0]}, {\[Sigma], 0, 7.5, 0.25}];
200  zzBE = Table[{\[Epsilon]yy[0, \[Sigma]],
201      sEgS[0, \[Sigma], 0]}, {\[Sigma], 0, 7.5, 0.25}];
```

Bibliography

[1] F. Wang, Z. Wang, Q. Wang, F. Wang, L. Yin, K. Xu, Y. Huang, and J. He, "Synthesis, properties and applications of 2d non-graphene materials," *Nanotechnology*, vol. 26, no. 29, p. 292001, 2015.

[2] Q. H. Wang, K. Kalantar-Zadeh, A. Kis, J. N. Coleman, and M. S. Strano, "Electronics and optoelectronics of two-dimensional transition metal dichalcogenides," *Nature nanotechnology*, vol. 7, no. 11, p. 699, 2012.

[3] F. Xia, H. Wang, D. Xiao, M. Dubey, and A. Ramasubramaniam, "Two-dimensional material nanophotonics," *Nature Photonics*, vol. 8, no. 12, p. 899, 2014.

[4] H. O. Churchill and P. Jarillo-Herrero, "Two-dimensional crystals: Phosphorus joins the family," *Nature nanotechnology*, vol. 9, no. 5, p. 330, 2014.

[5] A. Rodin, A. Carvalho, and A. C. Neto, "Strain-induced gap modification in black phosphorus," *Physical review letters*, vol. 112, no. 17, p. 176801, 2014.

[6] Q. Wei and X. Peng, "Superior mechanical flexibility of phosphorene and few-layer black phosphorus," *Applied Physics Letters*, vol. 104, no. 25, p. 251915, 2014.

[7] X. Ling, H. Wang, S. Huang, F. Xia, and M. S. Dresselhaus, "The renaissance of black phosphorus," *Proceedings of the National Academy of Sciences*, vol. 112, no. 15, pp. 4523–4530, 2015.

[8] S. Nakajima, Y. Toyozawa, and R. Abe, *Physics of elementary excitations*. Springer-Verlag, 1980.

[9] M. P. Marder, *Condensed matter physics*. John Wiley & Sons, 2010.

[10] T. Kazimierczuk, D. Fröhlich, S. Scheel, H. Stolz, and M. Bayer, "Giant rydberg excitons in the copper oxide cu 2 o," *Nature*, vol. 514, no. 7522, p. 343, 2014.

[11] L. Li, J. Kim, C. Jin, G. J. Ye, D. Y. Qiu, H. Felipe, Z. Shi, L. Chen, Z. Zhang, F. Yang, *et al.*, "Direct observation of the layer-dependent electronic structure in phosphorene," *Nature nanotechnology*, vol. 12, no. 1, p. 21, 2017.

[12] V. Tran, R. Fei, and L. Yang, "Quasiparticle energies, excitons, and optical spectra of few-layer black phosphorus," *2D Materials*, vol. 2, no. 4, p. 044014, 2015.

[13] P. Cudazzo, I. V. Tokatly, and A. Rubio, "Dielectric screening in two-dimensional insulators: Implications for excitonic and impurity states in graphane," *Physical Review B*, vol. 84, no. 8, p. 085406, 2011.

[14] A. Rodin, A. Carvalho, and A. C. Neto, "Excitons in anisotropic two-dimensional semiconducting crystals," *Physical Review B*, vol. 90, no. 7, p. 075429, 2014.

[15] P. G. Ciarlet and J.-L. Lions, *Handbook of numerical analysis*, vol. 8. Gulf Professional Publishing, 1990.

[16] A. Rohatgi, "Webplotdigitizer: Web based tool to extract data from plots, images, and maps." https://automeris.io/WebPlotDigitizer/.

[17] L. Wang, A. Kutana, X. Zou, and B. I. Yakobson, "Electro-mechanical anisotropy of phosphorene," *Nanoscale*, vol. 7, no. 21, pp. 9746–9751, 2015.

[18] S. P. Koenig, R. A. Doganov, H. Schmidt, A. Castro Neto, and B. Özyilmaz, "Electric field effect in ultrathin black phosphorus," *Applied Physics Letters*, vol. 104, no. 10, p. 103106, 2014.

[19] J. Pereira Jr and M. Katsnelson, "Landau levels of single-layer and bilayer phosphorene," *Physical Review B*, vol. 92, no. 7, p. 075437, 2015.

[20] D. Midtvedt, C. H. Lewenkopf, and A. Croy, "Multi-scale approach for strain-engineering of phosphorene," *Journal of Physics: Condensed Matter*, vol. 29, no. 18, p. 185702, 2017.

[21] J.-H. Choi, P. Cui, H. Lan, and Z. Zhang, "Linear scaling of the exciton binding energy versus the band gap of two-dimensional materials," *Physical review letters*, vol. 115, no. 6, p. 066403, 2015.

[22] H. Liu, A. T. Neal, Z. Zhu, Z. Luo, X. Xu, D. Tománek, and P. D. Ye, "Phosphorene: an unexplored 2d semiconductor with a high hole mobility," *ACS nano*, vol. 8, no. 4, pp. 4033–4041, 2014.

[23] V. Tran, R. Soklaski, Y. Liang, and L. Yang, "Layer-controlled band gap and anisotropic excitons in few-layer black phosphorus," *Physical Review B*, vol. 89, no. 23, p. 235319, 2014.

[24] J. Yang, R. Xu, J. Pei, Y. W. Myint, F. Wang, Z. Wang, S. Zhang, Z. Yu, and Y. Lu, "Optical tuning of exciton and trion emissions in monolayer phosphorene," *Light: Science & Applications*, vol. 4, no. 7, p. e312, 2015.

[25] X. Wang, A. M. Jones, K. L. Seyler, V. Tran, Y. Jia, H. Zhao, H. Wang, L. Yang, X. Xu, and F. Xia, "Highly anisotropic and robust excitons in monolayer black phosphorus," *Nature nanotechnology*, vol. 10, no. 6, p. 517, 2015.

[26] L. Liang, J. Wang, W. Lin, B. G. Sumpter, V. Meunier, and M. Pan, "Electronic bandgap and edge reconstruction in phosphorene materials," *Nano letters*, vol. 14, no. 11, pp. 6400–6406, 2014.

[27] T. Low, R. Roldán, H. Wang, F. Xia, P. Avouris, L. M. Moreno, and F. Guinea, "Plasmons and screening in monolayer and multilayer black phosphorus," *Physical review letters*, vol. 113, no. 10, p. 106802, 2014.